Article:
Birch, CE, Parker, DJ, O'Leary, A et al. (4 more authors) (2013) Impact of soil moisture and convectively generated waves on the initiation of a West African mesoscale convective system. Quarterly Journal of the Royal Meteorological Society, 139 (676). pp. 1712-1730. ISSN 0035-9009

https://doi.org/10.1002/qj.2062

Quarterly Journal of the
Royal Meteorological Society

The impact of soil moisture and convectively-generated waves on the initiation of a West African mesoscale convective system

Journal:	*QJRMS*
Manuscript ID:	QJ-12-0088.R2
Wiley - Manuscript type:	Research Article
Date Submitted by the Author:	n/a
Complete List of Authors:	Birch, Cathryn; University of Leeds, Institute for Climate and Atmospheric Science Parker, Doug; University of Leeds, Institute for Climate and Atmospheric Science O'Leary, Aaron; University of Leeds, Institute for Climate and Atmospheric Science Marsham, John; University of Leeds, National Centre for Atmospheric Science Taylor, Christopher; Centre for Ecology and Hydrology, Harris, Phil; Centre for Ecology and Hydrology, ; Lister, Grenville; University of Reading, National Centre for Atmospheric Science
Keywords:	Mesoscale convective system, Secondary initiation, Gravity wave, Soil moisture, Land-atmosphere interaction, AMMA

The impact of soil moisture and convectively-generated waves on the initiation of a West African mesoscale convective system

C. E. Birch[1], D. J. Parker[1], A. O'Leary[1], J. H. Marsham[2], C. M. Taylor[3], P. Harris[3], G. Lister[4]

C. E. Birch, Institute for Climate and Atmospheric Science, School of Earth and Environment, University of Leeds, Leeds, LS2 9JT, UK. (C.E.Birch@leeds.ac.uk)

[1]Institute for Climate and Atmospheric Science, School of Earth and Environment, University of Leeds, Leeds, LS2 9JT, UK

[2]National Centre for Atmospheric Science (NCAS), School of Earth and Environment, University of Leeds, Leeds, LS2 9JT, UK

[3]Centre for Ecology and Hydrology, Wallingford, UK

[4]NCAS, Department of Meteorology, University of Reading, Reading, RG6 6AH, UK

Keywords: mesoscale convective system (MCS), secondary initiation, gravity wave, soil moisture, AMMA

Abstract

A mesoscale convective system (MCS) case study was observed over northeast Mali as part of the African Monsoon Multidisciplinary Analysis (AMMA) on 31st July 2006. Observations of this case suggest that the soil-moisture heterogeneity and atmospheric gravity waves emitted from a 'parent' MCS were important trigger mechanisms for this system. This study uses high resolution Met Office Unified Model (MetUM) simulations to assess the importance of the synoptic circulation, land-surface and gravity waves in the initiation and development of the MCS. During the early afternoon shallow convection developed over a region of dry soil within a synoptic-scale convergence zone, which was caused by the confluence of the southerly monsoon flow with winds associated with the circulation around the Saharan heat low. Two pronounced waves were emitted from a nearby 'parent' storm and propagated towards the convergence zone. When the second wave reached the location of the shallow convection, deep convection was immediately initiated. Further convective cells developed later in the afternoon over dry soil, many adjacent to strong soil moisture gradients; these aggregated with the main storm, which later developed into the case study MCS. A comparison of model simulations with/without the soil moisture heterogeneity and gravity waves shows that the synoptic-scale circulation and convergence zones, specified by the atmospheric analysis was the most important factor for the successful simulation of the MCS. If the detailed location of the initiation of the system is to be forecast accurately, the land-surface, i.e. the soil moisture, must be adequately represented. In order to reproduce the timing of the secondary initiation of convection correctly the model must be able to capture gravity waves that are emitted by existing systems.

1 Introduction

1.1 Convection and land-surface interaction over West Africa

The Sahel region of West Africa receives 80-90% of its annual rainfall through convective clouds, mainly in the form of mesoscale convective systems (MCS's) (Laurent et al., 1998; Mathon et al., 2002). The Sahel has suffered serious droughts during recent decades (Janicot et al., 2008) and therefore, it is important that rainfall variability can be predicted on various timescales. There are currently problems with rainfall prediction over West Africa both at numerical weather prediction (Meynadier et al., 2010; Agustí-Panareda et al., 2010c) and at climate scales (Hourdin et al., 2010). MCS's are a particular problem in global models because accurate representation of their trajectories, propagation speed and precipitation distribution requires the explicit treatment of moist convection.

Taylor et al. (1997) and Koster et al. (2004) show that in semi-arid regions such as West Africa, soil moisture has a strong influence on precipitation. Moist convection requires both a humidity and heat source. Compared to dry soil, the boundary layer is cooler and moister over wet patches (Kohler et al., 2010). In a one-dimensional framework, fluxes of equivalent potential temperature are almost independent of Bowen ratio (as discussed by Garcia-Carreras, 2011) and it is therefore unclear, *a priori,* whether new convection will form over hot, dry or wet, cool surfaces. Observations have shown that new convective cells generally initiate preferentially over surfaces with locally enhanced sensible heat fluxes, i.e. over warm, dry soil (Carleton et al., 2001; Negri et al., 2004; Taylor and Ellis, 2006; Wang et al., 2009); in the case of soil moisture, this implies a negative soil moisture-precipitation feedback. One reason for this is that although over wet soils the lower sensible heat fluxes reduce entrainment of low equivalent potential temperature air, which increases convective available potential energy (CAPE), the shallower convective boundary layer (CBL) with a strong lid

tends to lead to higher convective inhibition (CIN, Adler et al., 2011; Garcia-Carreras et al., 2011). Soil moisture heterogeneity can cause horizontal gradients in near-surface temperature, which can generate mesoscale circulations analogous to a land-sea breeze (Segal and Arritt, 1992). These circulations can cause moisture convergence and a minimum in the entrainment-dilution of CBL air (Taylor et al., 2007; Adler et al., 2011; Garcia-Carreras et al. 2011), favouring deep convection during the afternoon (Emori, 1998). For these reasons, the optimum location for convection initiation appears to be on dry soil that is adjacent to strong gradients in soil moisture (Taylor et al., 2011).

Whilst the soil moisture-precipitation feedback appears to be negative in the early stages of convection, when the system is in its mature stage the feedback can be positive (Gantner and Kalthoff, 2010). Taylor and Lebel (1998) use a dense network of rain gauges to show that there was a strong preference for increased rainfall at stations where it had rained in the last 2-3 days. Similarly, Wolters et al. (2010) show using a mesoscale weather model that precipitation intensity is greater over wet soil. Convective systems become more intense over wet soil due to the increased availability of moisture and CAPE at the surface (Taylor and Clark, 2001; Gantner and Kalthoff, 2010).

Representation of the soil moisture-precipitation feedback in models is uncertain (Gaertner et al, 2010) because soil moisture is not well represented (Agustí-Panareda et al., 2010a; Agustí-Panareda et al., 2010b) and there are large biases in the water budget (Meyandier, 2010). Soil moisture is also not the only precipitation trigger mechanism. Klüpfel et al. (2011a) used high-resolution simulations to assess the impact of a number of soil moisture fields on precipitation in the Sahel and Sudan regions. They concluded that although there were major variations in the precipitation produced in the simulations, the timing of convection initiation was mainly influenced by the atmospheric forcing. A similar result was

found by Guichard et al. (2010), who found that the conditions used to initialise both mesoscale and global models had a significant control on the location of rainfall at synoptic scales.

1.2 Secondary initiation of storms

There are three possible mechanisms for the secondary initiation of convection over West Africa: 1) dynamical lifting by cold pools, 2) waves in the form of a bore or solitary wave, which are induced by the cold pool, and 3) waves that are generated by the updrafts within a convective system and propagate horizontally in a waveguide. Storm outflows, caused by evaporatively cooled downdrafts, are analogous to gravity currents (Charba, 1974; Mueller and Carbone, 1987). Cold air slumps downwards to the surface in the storm and then spreads out radially. The gust front (leading edge of the cold pool) is marked by a region of low-level convergence and ascent (Charba, 1974; Goff, 1976). These fronts can trigger deep convection by dynamically forcing the top of the boundary layer to ascend (Emanuel, 1994; Xue et al., 1997; Lin et al., 1998; Lothon et al., 2011) or by the collision of two mature cold pools (Droegemeier and Wilhelmson, 1985a, 1985b; Tompkins, 2001).

Gravity currents can generate a bore or solitary wave in front of the current head, which propagates along interfaces between fluids of different densities (e.g. Crook and Miller, 1985; Rottman and Simpson, 1989; Knupp, 2006). Such waves have been observed to propagate on the surface nocturnal inversion layer in US storm case-studies (Koch et al., 2008), or on the elevated stable layer remaining after the passage of a sea-breeze flow in Australia (Smith, 1988; Goler and Reeder, 2004). Such waves can travel faster than the head of the current and unlike the cold pool, they are not directly eroded by the heat fluxes at the surface, which means the waves can propagate much further in the horizontal than the gravity current (Ross et al. (2004) describe the erosion of gravity currents in this way). However, there is currently

no clear evidence of daytime solitary waves in the Sahelian environment either from observational or model studies.

Cloud systems or MCS's generate waves that can either enhance or suppress further convection in the region surrounding the 'parent' storm (Mapes, 1993; Liu and Moncrieff, 2004). Tropospheric gravity waves emitted from mid-latitude MCS's and their impact on convection triggering and organisation is reasonably well documented (e.g. Raymond, 1983; Uccellini and Koch, 1987; Stobie et al., 1983; Marsham and Parker, 2006). Over the tropics deep convection is at a maximum (Pfister et al., 1993) and the influence of the resulting gravity waves is larger due to the reduced effect of the Coriolis force (Liu and Moncrieff, 2004). Stensrud and Fritsch (1993, 1994) and Anabor et al. (2009) suggest that it is the combined effect of internal gravity waves and cold pools that control the upstream propagation of MCS events. Gravity waves lead to the initial upstream development of convection, but once it is established and cold pools begin to form, it is the cold pools that dominate the subsequent convective development.

The majority of the previous work on secondary initiation has been performed using idealised, cloud-resolving simulations (e.g Lane and Reeder, 2001; Beres et al., 2002; Song et al., 2003; Lane and Zhang, 2011). There have only been a handful of observed cases that have been studied in an atmospheric model (Piani et al., 2000; Lac et al., 2002; Morcrette et al., 2006; Marsham and Parker, 2006). None of these cases have been over West Africa. Bretherton and Smolarkiewicz (1989) show that linear tropospheric gravity waves propagate radially from convective clouds, providing compensating subsidence for the updrafts within the cloud system. Mapes (1993) applied this idea to MCS's in the tropics, where wind shear is weak for much of the time. He showed that a prescribed heat source (like an MCS) can generate horizontally propagating bores, which have vertical wavelengths that are harmonics of the depth of the waveguide. The n=1 wave mode has a vertical wavelength equal to twice

the depth of the waveguide; it travels fast and induces deep subsidence. The n=2 and n=3 wave modes can induce ascent in the lower troposphere, which produces favourable conditions for new convection.

1.3 Case study background

Observations of the mesoscale convective system used in this case study are described in detail by Taylor et al. (2010). They describe the initiation and development of the storm using in-situ aircraft, dropsonde and satellite observations made during the AMMA (African Monsoon Multi-disciplinary Analysis) field campaign (Redelsperger et al., 2006). The storm initiated in northeast Mali at approximately 13Z, 31st July 2006 and propagated westwards, until it decayed off the west coast of Africa on 2nd August.

Taylor et al. (2010) describe two important factors for the initiation and development of the system: 1) the distribution of wet and dry soil in the region of the initiation and 2) the influence of an atmospheric wave, emitted by a mature 'parent' storm (marked 'P' on Figure 1) that was situated ~250 km to the south. The case study ('daughter') storm initiated at 16.5°N, 1°E over an area of dry soil (marked 'D' on Figure 1) that was within a wetter region created by the passage of a MCS on the previous day (30th July 2006). The initiation point was adjacent to a strong soil moisture gradient, upwind of a wet patch. Taylor et al. (2010) show that boundary-layer air over the wet patch was cooler than over the dry soil and suggest that this induced a mesoscale circulation similar to a sea breeze, which initiated shallow convection.

Evidence for the atmospheric wave was found in satellite retrievals of brightness temperature, in the form of a band of cloud that was observed to propagate outwards from the parent storm at a speed of ~13 m s^{-1}. This wave reached the daughter storm at approximately 13Z, coinciding with the development of deep convection and high cloud (see green lines in Figure

16). It was not clear from the observations whether the wave took the form of a solitary wave (bore) or a wave-front. The authors suggest that a bore could propagate along the stable interface between the CBL and the near-neutral Saharan Air Layer (SAL). Any upward displacement of air caused by the bore could readily generate new convection because, compared to the stratified free-troposphere, the neutrality of the SAL means only a small amount of energy would be needed to produce enough uplift to bring air to its level of free convection. The temperature of the cloud band in the satellite observations did however suggest that the observed clouds were at a much higher altitude than the CBL-SAL interface, suggesting that the wave feature was not confined to low-levels and could have taken the form of a wave-front instead.

Klüpfel et al. (2011b) used COSMO (Consortium for Small-scale Modeling) simulations at 2.8-km resolution, with explicit deep convection to study the 31st July 2006 MCS case. The simulations suggest that the important triggering mechanisms for the daughter storm were: 1) mesoscale circulations resulting from soil moisture heterogeneities and 2) larger-scale convergence zones at the initiation location. The parent and daughter storms were reproduced in the simulations, but both appeared approximately 9 hours too late and 100-150 km too far south. The model simulations showed that a cyclonic vortex to the north-east caused westerly winds in the CBL over the initiation location on 31st July. During early afternoon precipitating cells formed but did not develop into a larger system because there was no large-scale moisture supply. Later in the day the parent storm moved in from the west, and cooling by the evaporation of rainfall generated a strong density current that propagated northwards. The easterly/south-easterly winds from the cold pool intensified the southerly monsoon flow and converged with the westerly winds associated with the vortex to form a convergence zone north of the parent storm. The reinforced southerly winds also transported moist monsoon air northwards, which reached the daughter initiation location by late

evening. At this time deep convection was initiated, which eventually developed into the daughter MCS.

Klüpfel et al. (2011b) conclude that the most important triggering mechanism was the low-level synoptic-scale convergence, reinforced by the density current. They do however state that the relative importance of the various triggering mechanisms in the simulations is questionable due to the 9 hour difference in the initiation time between the observations and model; the mesoscale circulations may have had a greater influence if the modelled storm had initiated during the day, as observed in reality.

The aim of this study is to use high-resolution, convection-permitting model simulations to study the initiation and development of the daughter storm. One of the simulations uses realistic soil moisture patterns, derived from observations, to assess the importance of land-surface variability on the initiation location of the storm. The simulations are also used to characterise the observed atmospheric wave and to determine the importance of waves as a trigger mechanism.

2 Model experiments and set-up

The model simulations were performed using version 7.3 (Parallel Suite 22) of the Met Office Unified Model (MetUM). The MetUM has a semi-Lagrangian, semi-implicit and non-hydrostatic formulation and a terrain-following co-ordinate system (Davies et al., 2005). Many types of process are parameterised, such as the surface (Essery et al., 2001), the boundary layer (Lock et al., 2000) and mixed-phase cloud microphysics (Wilson and Ballard, 1999). Convection is parameterised in the global and 12-km nest using the Gregory and Rowntree (1990) scheme and convection is explicit in the 4-km simulations.

The global model was initialised using operational European Centre for Medium-Range Weather Forecasts (ECMWF) analyses and is used to create lateral boundary conditions for the 12-km resolution (50 vertical levels) nest. The 12-km nest creates lateral boundary conditions and initial conditions for the 4-km resolution (70 vertical levels) nest. The thick black boxes in Figure 1 show the location and size of the 12 and 4-km domains. Figure 2 illustrates the various model simulations that were performed. The model was initialised at 12Z on both 30th and 31st July 2006 and at 00Z on 30th July 2006 using ECMWF analyses.. The best results were obtained using the 12Z 30th analysis (see section 3a for more details) and this simulation is therefore designated as the `control'. A restart dump from the 4-km nest was obtained from the control simulation at 06Z on the 31st July 2006. A separate experiment was then initialised with this dump, together with a more realistic soil moisture distribution (`ASSIM'), and run until 21Z on the 31st July 2006.

The fine horizontal resolution ASSIM soil moisture field was created by running an off-line simulation of the MetUM's land surface scheme (Joint UK Land Environment Simulator, JULES; Best et al., 2011), constrained by 3-km resolution satellite observations of land surface temperature (LST) from the EUMETSAT Land SAF (Satellite Applications Facility; Trigo et al. 2008). This JULES simulation was forced with 0.5° near-surface boundary conditions provided by the AMMA Land Surface Model Intercomparison Project, ALMIP (Boone et al., 2009), along with satellite-derived 0.1° rainfall estimates from EPSAT-SG (Estimation of Precipitation by Satellite – Second Generation; Bergès et al, 2010). The model was constrained daily by adjusting non-zero EPSAT-SG rainfall amounts for each 3 km pixel to give the root-mean-squared best fit between modelled and observed LST, yielding a fine resolution soil moisture estimate on the domain (10-20°N, 10°W-10°E) at 0.0275° (~3 km) resolution. This model-derived estimate was favoured over the use of a satellite-derived soil moisture product (e.g., from AMSR-E, Advanced Microwave Scanning Radiometer – Earth

Observing System) for several reasons: (1) the satellite products only provide information on the moisture content of the uppermost soil layer, whereas JULES computes the moisture on all four of the MetUM's soil levels; (2) data from AMSR-E are available typically once per day, so new soil moisture features created after the overpass time are not captured; (3) AMSR-E soil moisture resolves features on scales of ~50 km, but Taylor et al. (2011) show that the dominant influence of soil moisture on convective initiation occurs at finer length scales; and (4) the modelled surface energy budget is influenced more by the soil moisture content relative to model parameters (the volumetric saturation, critical and wilting points) than by the absolute amount of water in the soil. Regarding this last point, the gridded datasets of these soil parameters that are available for our West African domain are constrained by few observations compared to other regions in the world. They exhibit unrealistic, coarse scale spatial discontinuities, which, when used in JULES, dominate the spatial variability in the modelled land surface state and fluxes over the variability produced by the fine scale variation in land cover type and soil moisture. For this reason, the ASSIM soil moisture was computed by JULES using spatially uniform values for these parameters (saturation point = 0.4036 $m^3 m^{-3}$, critical point = 0.2175 $m^3 m^{-3}$ and wilting point = 0.1152 $m^3 m^{-3}$), and the same uniform values were used in the subsequent MetUM simulations. Note that the other soil parameters, such as the soil thermal conductivity and thermal capacity, were also set to constant, relevant values as identified during ALMIP. The ASSIM soil moisture field was averaged onto the 4 km MetUM grid, smoothed at the boundaries towards the model soil moisture values and merged with the 4 km restart dump. Both the ASSIM soil moisture field and the MetUM have 4 soil layers with thicknesses of 0.1 (uppermost), 0.25, 0.65 and 2.0 m.

3 Results

3.1 Evolution of the simulated MCS's

An overview of the synoptic conditions at 12Z, 31st July 2006 is shown in Figure 1. The African Easterly Jet is weak at this time and lies at approximately 11°N. The trough axis of an African Easterly Wave lies at 4°E, between 8 and 20°N. The winds at 700 hPa are predominantly north-easterly over the MCS initiation location, which is marked by the 'D' in Figure 1.

Figure 3 uses 6-hourly accumulated precipitation derived from the control model simulation and from the TRMM3B42 satellite rainfall product (TRMM, Tropical Rainfall Measuring Mission, Huffman et al. (2007)) to illustrate the initiation and development of the systems associated with this case study. The observations show that an MCS developed on the 30th July and produced a large amount of rainfall during the evening of the 30th and early morning of the 31st July (black circles in Figure 3a-b). This system created patches of wet soil in the region 13-18°N, 4°W-3°E. The parent storm initiated on the afternoon of the 30th between 10-15°N, 5-10°E and tracked westwards until it dissipated during the afternoon of the 31st between 2°W and 2°E (red circles in Figure 3a-d). Even though the details of the model rainfall distribution do not agree well with the observations, the timing, general location and propagation of these two systems are reproduced well by the model (i.e. within 1° and 1 hour, Figures 3g-j).

The daughter MCS initiated during the afternoon of the 31st July at 16°N, 1°E, developed into a MCS during late afternoon and then propagated towards the west on 1st August (marked by the green circles in Figure 3d-f). The system reached the west coast of Africa on 2nd August and began to dissipate (not shown). Again, the model control simulation reproduces the timing, general location and propagation of this system with good accuracy (Figure 3j-l), but the details of the initiation are different to those suggested by the observations.

Hovmöller plots of hourly precipitation rates, averaged between 11 and 18°N, for both the TRMM3B42 and EPSAT-SG (Estimation of Precipitation by SATellite Second Generation, Bergés et al. (2010)) satellite products, and the various model simulations are shown in Figure 4. The TRMM3B42 product illustrates the westward propagation of the parent storm (P) between 12Z 30th and 12Z 31st July, followed by the initiation and propagation of the daughter storm (D). The system to the west (WP), which produced the patches of wet soil between 4°W and 3°E is also shown in the satellite precipitation. The EPSAT-SG data has a higher temporal and spatial resolution than the TRMM3B42 data and it is derived from a combination of TRMM data, GPCP-1dd (Global Precipitation Climatology Project) data and multiple channels from the SEVIRI (Spinning Enhanced Visible and Infrared Imager) instrument on the MSG (Meteosat Second Generation) satellite. The propagation of the three systems in the EPSAT-SG product is very similar to that in the TRMM3B42 product, giving confidence in the use of TRMM3B42 data for the comparisons with the model.

Figure 4c and d show rainfall rates from the control and ASSIM simulations. As shown in Figure 3, the control simulation successfully reproduces the initiation and propagation of the parent and daughter storms. Rainfall from the model simulation that was initialised with an analysis 24 hours later (12Z 3st July) than that used in the control simulation is shown in Figure 4e. The daughter storm is reproduced in this run but the parent storm is absent: the rainfall develops approximately 5 hours too late and the system propagates too slowly westwards on 1st August. Figure 4f shows rainfall diagnostics from the simulation initialised at 00Z 31st July. This run is less successful than the runs initialised at 12Z; the rainfall pattern does not resemble the signature of the daughter storm at all.

The reasons for the differences between the simulations are illustrated using plots of 925 hPa potential temperature, specific humidity, winds and convergence at 12Z, 31st July (Figure 5). In the control simulation and the simulation initialised at 12Z 31st July the daughter storm

develops in a region of synoptic scale convergence (marked by the black contour lines and the 'D' in Figures 5a and b respectively). This convergence zone forms through the confluence of the moist, southerly winds associated with the parent storm ('P') and the westerly winds associated with the cyclonic circulation around the heat low. The leading edge of the simulated cold pool produced by 'P' is more than 100 km to the southeast of the daughter storm initiation point at 12Z, 31st July (e.g. see Figure 16 and associated discussion) and therefore cannot directly influence this convergence zone. Klüpfel et al. (2011b) conducted a sensitivity simulation of this case, in which the evaporative cooling is removed from their simulation, which suppresses the cold pool from the parent storm. They demonstrate from this that the parent storm does indeed modify the southerly monsoon flow and is a significant factor in the development of this low-level convergence zone, but this is not caused directly by the cold pool.

The synoptic circulation in the simulation initialised at 00Z 31st July (Figure 5e,f) is different to the two simulations described above. Neither the parent storm nor the southerly winds north of it are reproduced by the model and therefore, the large-scale convergence zone does not develop. Without this convergence zone the daughter storm is not reproduced (Figure 4f).

3.2 Land-atmosphere interaction

In this section the influence of soil moisture on the initiation of the daughter MCS is investigated through a comparison between the control and ASSIM simulations. Figure 6a shows soil moisture at 13Z, 31st July 2006, derived from the EPSAT-SG rainfall product and the AMSR-E brightness temperatures (Pellarin et al., 2009). This product is produced by estimating soil moisture from a high spatial and temporal resolution rainfall product and then the AMSR-E brightness temperatures are used to account for uncertainties in the rainfall. The satellite product shows mainly wet soil south of 12.5°N, a patch of wet soil in the region 13-

18°N, 3°W-2°E and drier soil around 16.5°N, 0.5°W and 13-15°N, 1-4°E. The control run has a distinctive large-scale north-south gradient in soil moisture that is a result of the ECMWF analysis (Figure 6e); soil moisture decreases between 10 and 13°N, there are very low values between 13 and 17°N and larger values in the north-east of the sub-domain, which is associated with a region of slightly elevated orography. The wet patch at 14-16°N, 5°W-1.5°E was created by the MCS on the previous day and the wet patch at 11-13°N, 3-5°E was created by the parent MCS. The ASSIM soil moisture (Figure 6i) bears more resemblance to the observations than that in the control run due to the large amount of satellite data used to produce the ASSIM soil moisture product. The observed north-south gradient and the wet patch centred at 13-18°N, 3°W-2°E is reproduced and like the satellite-derived soil moisture, there is a dry patch centred at 14.5°N, 2°E and a small dry patch, surrounded by wet soil at 16.5°N, 0.5°W.

Figure 6b-d shows MSG brightness temperatures, where white shading depicts cold, high cloud. At 13Z, 31st July 2006 the parent storm is clearly visible in the satellite imagery (marked with a blue 'P'); it then tracked westwards during the afternoon, reaching 3°W by 18Z. The location of the daughter storm is illustrated on Figure 6c and d (marked with a blue 'D'); it initiated over relatively dry soil, with a wet patch of soil immediately to the southeast and an additional wet patch approximately 80 km to the northwest (shown in more detail in Figure 3, Taylor et al. (2010)). By late afternoon (Figure 6d) the daughter storm had increased in size and most of the subsequent convection in the system occurred over wet soil (Taylor et al., 2010).

The position and propagation of the parent storm is similar in the control and ASSIM runs. Between 13Z and 15Z the simulated parent storm is 120-150 km to the east of the observed parent storm and dissipates too early in the afternoon. The daughter storm in both of the model simulations initiates at 13Z over dry soil at 15°N, 1-3°E, approximately 170 km to the

south-east of the observed storm. The subsequent evolution of the storm in the model simulations differs to that in the observations. The satellite imagery suggests that the daughter storm initiates at a single point and then develops. In the model simulations the daughter storm grows in size by the accumulation of many individual convective cells, which develop later than the main daughter storm (Figure 6h and l). These additional cells form on the dry soil but mainly close to the boundaries of the substantial wet patch. The exact location of these cells differs in the control and ASSIM simulations because the wet patches differ in their position.

The initiation times and locations of the new convective cells in relation to the soil moisture heterogeneity is shown in more detail in Figure 7. The times were diagnosed subjectively using hourly plots of model rainfall rate. When the rainfall rate associated with a particular cell became continuous over two 1-hour time intervals, and prevailed over a region with a radius greater than ~20 km, an initialisation time and location was noted on the plot. The preference for initiation over soil-moisture gradients is similar in the two runs, but slightly less widespread in the ASSIM run, which is more consistent with the observations.

In Figure 7, the initiation point of the main daughter storm is marked by '14Z' at 14.8°N, 2°E in both the control and ASSIM simulations. The location of the parent storm at 12Z is shown on the plots by the thick white contour at 12-14°N, 1-3°E. The daughter storm initiates over a region of dry soil, which is in the same location as the significant boundary-layer convergence cause by the confluence of the moist southerly monsoon winds with the westerly winds to the south of the Saharan heat low.

The differences in boundary-layer structure over the wet and dry soil are illustrated by a tephigram of model diagnostics at 11Z, 31st July (Figure 8). Over the dry soil (at 15°N, 1.7°E, solid lines) the boundary layer is deeper (extends to 850 hPa, compared with 925 hPa) and

~6°C warmer than over the wet soil (16°N, 1°E). Contrary to what would be expected, the lower atmosphere (925 to 650 hPa) is more humid over the dry soil than over the wet soil. This increase in low-level humidity is caused by the monsoon flow, which transports moist air from the south. The monsoon flow does not reach the location of the wet soil (16°N, 1°E in Figure 8) and thus the humidity at that location is lower. The higher temperatures (and to a much lesser extent the humidities) over the dry soil cause the CAPE to be approximately double that of the wet soil (1074 J kg^{-1}, compared to 529 J kg^{-1}). CIN is also much lower over the dry soil (16 J kg^{-1}, compared to 163 J kg^{-1}). The low CIN, high CAPE combination of the monsoon air over the dry soil provides suitable conditions for the development of deep convection. It was this thermodynamic profile and the uplift provided by the convergence zone that initiated the convection that later developed into the daughter storm.

The other convective cells initiate later (mainly at 17 and 18Z, Figure 7), over dry soil, with many developing adjacent to strong gradients in soil moisture. These cells occur due to boundary-layer convergence that develops as a result of the mesoscale circulations, which are caused by the difference in boundary-layer temperatures over the wet and dry soil. These cells initiate later than the daughter storm because they are largely outside the synoptic-scale convergence zone and therefore, the mesoscale circulations require time to develop.

Figure 9 illustrates the change in a number of model diagnostics along a southeast to northwest transect (shown by the straight lines in Figures 5 to 7). This transect was designed to incorporate both the parent and daughter storm locations, as well as the wet patch at 16°N. The location of the parent storm at 11Z in both the control and ASSIM simulations is between 11 and 13°N, which is shown by the model medium cloud fraction in Figure 9a. This storm is precipitating and thus there is wet soil beneath it (Figure 9b). The region of wet soil produced by the MCS on the previous day is at 16°N. The soil moisture gradients are greater in the control run; the wet patch spans only ~100 km, compared to more than 300 km in the

ASSIM experiment. Moisture at the surface has a strong influence on the surface turbulent heat fluxes (Figure 9c). In the control run the sensible heat flux (H) is low over the wet soil patch at 16°N and higher over the drier soil to the north. The latent heat flux shows the opposite trend; it is higher over the wet patch at 16°N and lower over the drier soil. The fluxes in the ASSIM simulation are more similar across the soil moisture gradients; both the sensible and latent heat fluxes vary by less than 150 W m^{-2} over the wet and dry soil.

The differences in soil moisture and surface turbulent heat fluxes induce variations in surface and near-surface temperature. In both simulations the temperatures are higher over the dry soil (Figure 9d), although there is a southeast-to-northwest gradient in temperature between 13.5 and 15.5°N. The variations in specific humidity are less distinct; the soil moisture patches appear to have less of a control on the humidity and the main trend is a southeast-to-northwest decrease, which is due to moisture advection from the south. (Figure 9e).

3.3 The cold pool outflow generated by the parent storm

The parent storm generated a cold pool outflow in the model, as observed by Taylor et al. (2010). The cold pool can be identified in several of the model diagnostics in Figure 9. The head of the cold pool is associated with a peak in 10 m wind speed, decrease in surface temperature and medium level cloud centred at 13.5°N (Figures 9f, d and a respectively) and with a reduction in specific humidity and an increase in surface fluxes behind this (approximately 0.25° to the south). These perturbations are similar to those observed by Taylor et al. (2010) (see Figure 6 of their paper) and those observed in other tropical oceanic cold pools (e.g. Fig. 18 in Tompkins (2001)). The passage of the current head decreases the CAPE and increases the CIN of the near-surface air (Figure 9g and h), which is largely caused by the changes in near-surface temperature and humidity that are induced by the cold pool.

Figure 10 shows Hovmöller plots of virtual potential temperature, θ_v, and specific humidity, q, at 20 m above ground level, along the southeast to northwest diagonal transect marked in Figures 5-7. The thick white contour shows 100 % medium cloud fraction, thus illustrating the location of the parent storm. In the region of dry soil (13-15.5°N) θ_v generally increases through the morning due to increased solar heating. The cold pool decreases the temperature of the near-surface air, it has a lifetime of ~3 hours and travels approximately 60 km at a speed of 6.9±0.5 m s^{-1} towards the northwest (white dashed line). By 13Z the large turbulent heat fluxes at the surface have greatly reduced its strength and north of 14.25°N any buoyancy decrease from the cold pool is undetectable. It is possible that the cold pool does not progress far past the edge of the wet soil at 13.5°N because the large sensible heat flux over the dry soil leads to a rapid mixing away of the density gradient.

The specific humidity Hovmöller plot (Figure 10b) shows that at 06Z the boundary-layer air over the dry soil (13.5-15°N) is more humid than over the wetter soil to the north. This is due to the strong southerly monsoon flow shown in Figure 5a. The high humidity persists through to the afternoon, except for the south-eastern edge, where the humid air is replaced by drier air in the cold pool.

3.4 The role of waves generated by the parent storm in triggering convection

The influence of the atmospheric waves emitted by the parent storm was found to be very similar in the control and ASSIM simulations. For this reason the remainder of the section uses diagnostics from only the control run to investigate the role of waves in the triggering of the daughter storm. Figure 11 shows plots of vertical velocity in the initiation region of the daughter storm at 09 and 11Z, 31st July 2006. The location of the parent storm ('P') is indicated by the region of significant up and downdrafts south of 13°N. The daughter storm initiation location is to the north of this and is marked on the plot by the black 'X'. Two

significant waves are emitted from the parent storm in the early hours of the morning. The first wave (W1, indicated by the line of positive vertical velocity and the black dashed line) is emitted at approximately 06Z and propagates away from the parent storm, towards the northwest. By 09Z it is approximately 100 km away from the daughter storm initiation location (Figure 11a). The second wave (W2) is emitted from the parent storm at approximately 09Z and also propagates towards the northwest. By 11Z W1 has reached the daughter storm initiation location and W2 is approximately 100 km to the southeast (Figure 11b).

The structure, propagation and effect of the waves is illustrated using plots of θ_v, vertical velocity and medium cloud fraction along the diagonal transect (Figures 12 and 13). At 08Z, 31st July 2006 the parent storm is between 12 and 13.5°N, which is shown by the high levels of medium cloud in Figure 12a and the region of intense up and downdrafts in Figure 12b. The wet soil associated with the parent storm is illustrated by the dashed line in Figure 12a and the wet patch to the northwest is also shown between 15.7 and 16.4°.

Away from the parent storm the boundary layer is 0.8 to 1 km deep at 08Z (Figure 12b). The peak in boundary-layer temperatures at the daughter storm initiation location (~14.9°N) and the minimum in boundary-layer temperatures over the wet soil patch (~16°N) are already evident. W1 is emitted from the parent storm at approximately 06Z and propagates towards the northwest (left to right in the diagonal transect plots) between 08Z and 10Z (Figures 12b-d). W1 extends from the top of the CBL up to at least 8 km and is most prominent in the parts of the atmosphere with higher stability, i.e. 1-3 km and above 5.5 km, on either side of the near-neutrally stratified SAL. W1 does not produce cloud as it propagates towards the northwest (solid lines, Figure 12a).

By 11Z a cooler, shallower boundary layer is evident over the wet patch between 15.5 and 16.5°N and the shallow convection associated with the daughter storm is readily seen at 14.9°N (Figure 13b). The extent of the cold pool associated with the parent storm is also shown in Figure 12d and Figure 13b-d. It does not propagate further north of 13.9°N. W1 reaches the region of shallow convection at approximately 11Z (14.8°N, Figure 13b). Cloud begins to form over this region between 11 and 12Z (black and red solid lines respectively, Figure 13a) but deep convection is not initiated at this time. W2 is emitted from the parent storm at approximately 09Z and is visible in Figure 13b at 14°N. This second wave also propagates towards the northwest and reaches the region of shallow convection at 14.8°N at 13Z. At this point deep convection is initiated and a large amount of cloud begins to form.

The structure of W1 and W2 is reasonably similar. Both waves cause upward displacement of air in the lower atmosphere (below 4 km for W1 and below 5.5 km for W2) and downward displacement of air in the upper troposphere. This has the potential to lift air parcels above their level of free convection and initiate deep convection.

Hovmöller plots of θ_v and medium cloud fraction, along the diagonal transect marked in Figures 5-7, at 2 and 6 km above mean sea level can be used to illustrate the propagation of the waves and their effect on the initiation of deep convection (Figure 14). The dashed white lines (labelled W1 and W2) indicate the propagation of the two waves, diagnosed from the Hovmöller plots themselves and an animation of cross-section plots at 5-minute intervals, similar to those in Figures 12 and 13. The parent storm is illustrated by the solid white contours between 11 and 13°N and the initiation of the daughter storm is shown by the white contours and black crosses at 14.9°N. W1 travels at 15.7±0.5 m s^{-1} (compared to Taylor et al. (2010)'s observed speed of ~13 m s^{-1}) and reaches the region of shallow convection at 11Z. The propagation of W1 causes upward displacement of air in the lower atmosphere (< 4km);

this is illustrated by the θ_v cross-sections in Figure 12 and by the lower values of θ_v behind the wave in Figure 14a.

Figure 15a shows a Hovmöller plot of CIN along the diagonal transect. Northwest of the parent storm (>13°N) CIN is reduced during the morning due to increased mixing caused by diurnal heating. W1 also decreases CIN, although the changes are only significant between 13 and 14.5°N. By the time W1 reaches the daughter storm initiation point (14.8°N) CIN is already very close to zero. Very low CIN is however, not the only prerequisite for the initiation of deep convection; a source of uplift is required. W1 does provide uplift but it does not provide enough to initiate deep convection at this time. It does however bring air to its lifting condensation level (LCL) and cloud begins to form (Figure 13a, red line). The influence of W1 on the LCL is illustrated in Figure 15b, which shows the actual pressure, p, at 3000 m above MSL, minus the pressure at which the air at 3000 m would have to be lifted to in order to reach its LCL, p_{LCL} i.e. when p - p_{LCL} is large the air at 3000 m is much lower (in altitude) than its LCL. As p - p_{LCL} decreases the air at 3000 m becomes closer to its LCL, until p - p_{LCL} = 0, at which point water in the air is able to condense and form clouds. This plot shows that W1 brings air at 3000 m to its lifting condensation level, i.e. provides enough uplift to allow shallow convection to commence.

The second wave (W2) propagates north-westwards at the faster speed of 19.3±0.5 m s^{-1}. Like W1, this wave also causes upward displacement of air in the lower atmosphere (Figure 14a) It reaches the region of shallow convection at 13Z, coinciding exactly with the development of deep convection (shown by the black crosses on Figure 14 and the development of a significant amount of medium cloud at 14.9°N). Compared to the first wave, the second wave arrives at a time when the mixing in the boundary layer is deeper and where shallow, moist convection already exists. W2 is therefore able to provide enough uplift to trigger deep convection.

An additional instance of wave-generated secondary initiation at 16.3°N at 16Z is illustrated in Figure 14b. A wave is emitted from the daughter storm between 14 and 15Z and propagates towards the region of shallow convection at 16.5°N (W3), which is over dry soil on the far side of the wet patch (shown in Figure 13). When this wave reaches the shallow convection at 16Z, the appearance of cloud in Figure 14b shows that deep convection is triggered. This wave is not evident in the θ_v field at 2 km because the waves only propagate in stratified regions of the atmosphere and by mid-afternoon the CBL extends to above 2 km.

3.5 The character of the convectively-generated waves

The schematic in Figure 16 summarises the propagation of the observed and simulated waves and cold pools. Deep convection in the observed daughter storm initiated in the region around 16.5°N, 1°E at 13Z. Taylor et al. (2010) suggest that this coincided with the arrival of a gravity wave that was emitted from the parent storm to the southeast (Figure 16, green lines). The only evidence for this wave was a band of high, cold cloud that was observed in the satellite imagery, which propagated north-westwards from the parent storm. There was also a cold pool associated with the observed parent storm, which also propagated towards the northwest, but at a slower rate compared to the wave (light grey dashed lines).

In the model simulation, deep convection associated with daughter storm developed at 13Z in the region 14.5°N, 2°E. Like the observations, this coincided with the arrival of a gravity wave (W2) from the simulated parent storm (Figure 16, blue lines). A cold pool was also simulated by the model, which like the observations, propagated towards the northwest but did not directly affect the initiation of deep convection in the daughter storm (dark grey dashed lines).

There are two main differences between the observed wave features and those simulated by the model. Firstly, the earlier wave in the model (W1, red lines) is not evident in the

observations. Either it did not occur in reality, or it did not produce sufficient cloud to be visible in the satellite imagery. Secondly, the location of the daughter storm and associated waves all occur approximately 100 km to the southeast of where they occurred in reality. The parent MCS in the model simulation was also approximately 100 km further south than the observed parent MCS at the time the waves were emitted (not shown). Although the location of the entire model parent-daughter system was displaced by some distance compared to ther observations, the speed of the model waves, the distance between the parent and daughter storm and the arrival time of the second wave (W2) at the daughter storm initiation location was in very good agreement with the observations.

Taylor et al. (2010) speculate about the type of wave that propagated outwards from the parent storm. The wave could have been either 1) a nonlinear 'bore' or solitary type wave, that was caused by the cold pool and propagated along the CBL and SAL interface, or 2) a wave-front that was not confined to the lower atmosphere. The θ_v and vertical velocity sections (Figures 12 and 13) and the Hovmöller plot in Figure 14b show that neither of the model waves were confined to low levels. They both produced upward displacement of air in the lower atmosphere (< 5 km) and downward displacement of air in the free troposphere (> 5.5 km). The waves in the model appear to take the form of a wave-front, rather than a bore that resides on the CBL-SAL interface. It is not possible to determine the exact structure of the wave from the satellite observations, although Taylor et al. (2010) suggest that the cloud associated with the wave is too cold (and therefore too high) to reside on the CBL-SAL interface. The model wave does not produce any cloud as it propagates northwestwards until is reaches the region of shallow convection associated with the parent storm. It is possible that either a) the model reproduces the wave structure as it occurred in reality but it does not produce the associated cloud or b) the wave structure in the model does not represent the exact observed structure.

The W1 and W2 waves in the simulation performed for this paper travel at similar speeds and appear to take the form of an n=2 mode wave. Like the n=2 mode in Lac et al (2002), but opposite to the n=2 waves in Lane and Reeder (2001) and Marsham and Parker (2006), the waves W1 and W2 cause upward displacement in the lower atmosphere and downward displacement in the upper atmosphere. The vertical wavelength (λ_z) of a wave can be estimated using the equation:

$$\lambda_z = \frac{n\pi c}{N}$$

where n is the wave mode, c is the phase speed and N is the Brünt-Väisälä frequency. Assuming n = 2, c = 17.5 m s $^{-1}$ (mean of the W1 and W2 speeds) and a mean value of N over the troposphere of ~0.01 s^{-1}, gives a vertical wavelength of ~11 km, which is approximately equal to the depth of the troposphere in this case.

A third wave is indicated on the θ_v Hovmöller plot at 6 km in Figure 14b (W0). It is emitted from the parent storm at approximately the same time as W1, but it travels faster (33.5±0.5 m s^{-1}, compared with 15.7±0.5 m s^{-1} for W1 and 19.3±0.5 m s^{-1} for W2). The maximum displacement occurs aloft and is therefore only visible in the 6 km Hovmöller plot. This wave may be the n=1 mode since it is approximately twice as fast (33.5 m s^{-1}) as the W1 and W2 waves.

4 The relative importance of the different triggering mechanisms

The model control simulation shows that the land surface and gravity waves are influential in the development of new convection. One of the additional simulations described in section 3.1, which was initialised at 12Z 31st July (24 hours later than the control), is a good test of the importance of these trigger mechanisms because it does not reproduce the soil moisture heterogeneity or the gravity waves associated with the parent storm.

Figure 17a shows the model soil moisture diagnostic at 13Z, one hour after the initialisation. The large-scale north-south soil moisture gradient is similar to that in the control, but the wet patch that was created by the MCS on the 30th is missing (compare to Figure 6e). Figure 17b to d show the development of the parent and daughter storms in this simulation. The parent storm is in the south of the domain and the daughter storm develops over the dry soil, in a location approximately 150 km to the northwest of the daughter storm in the control and in a position that is closer to that observed (compare Figure 17c with Figures 6c and g). The location is more accurate because the analysis gives a better representation of the synoptic-scale convergence zone. A sensitivity test was performed on the control, where the soil moisture was smoothed to its mean value over the region where the daughter storm initiated (not shown). In this case the daughter storm did not develop because the surface was not hot enough to produce deep mixing. It seems that the soil moisture patterns determine the exact structure of the developing storm but as long as there is some dry soil present, the synoptic-scale dynamics are a more important trigger mechanism.

The daughter storm in Figure 17 develops approximately 5 hours later in the day than in the control run and the observations. Although the parent storm is present in the simulation, no significant gravity waves are emitted from it (not shown). Time is required for convective-scale circulations to "spin-up" in the 4-km simulations, but this 5-hour delay in the formation of deep convection highlights the important role of the convectively-generated waves that triggered the storm in the control run. The analysis in section 3.4 shows that the arrival of a gravity wave coincides exactly with the initiation of deep convection. These waves may not be the determining factor in whether a storm is initiated or not, but they do influence the timing of the initiation of deep convection and therefore the timing of the development of a storm into a MCS.

These findings are in agreement with Guichard et al, (2010) who show that the initial and boundary conditions significantly control the locations of rainfall over West Africa and that explicit moist convection improves the precipitation distribution, MCS trajectory and propagation speed but cannot correct for weaknesses in the analysis. Klüpfel et al. (2011b) also suggest that the boundary-layer convergence zone was the most important triggering mechanism for this case. It seems that as long as there is some dry soil present, the synoptic-scale dynamics is the most important trigger mechanism, with the gravity wave from the parent storm and the soil moisture patterns being of secondary influence. If the model captures the large-scale environment accurately, the soil moisture heterogeneity determines the exact location of the initiation of the storm and the gravity waves determine the timing of the development of deep convection.

5 Summary

This study shows that the MetUM, run with explicit convection at 4-km horizontal resolution, is able to reproduce the key aspects of a mesoscale convective system (MCS) observed in the Sahel during summer (Taylor et al., 2010). The 4-km model simulations were very sensitive to the analyses used in the initialisation; two of the runs produced the case study well and one was unsuccessful. This appears to be due to differences in the way the analyses represent convergence zones caused by the confluence of cyclonic circulations around the Saharan heat low with the moist, southerly monsoon flow.

Similar to the observations, an MCS develops in the control simulation on the 30th July and creates the wet soil patches in the case study storm initiation region, before dissipating during the early hours of the 31st. A second MCS (the 'parent' storm) also develops on the 30th, although this persists through the night until the afternoon of the 31st. In the model the main 'daughter' storm develops at ~13Z on the 31st, over dry soil, in a synoptic-scale convergence

zone, enhanced by the circulation created by the parent MCS. Although this initiation appears less related to soil-moisture boundaries than in the observations of Taylor et al. (2010), other convective cells develop later in the afternoon (17 and 18Z) on dry soil, but adjacent to strong soil moisture gradients: the locations of these cells are consistent with boundary-layer convergence associated with mesoscale circulations caused by soil-moisture variations. During the evening the daughter storm and the other convective cells merge to form the case study MCS, whereas the observations show that the case study MCS initiated at one point and then grew in size.

Taylor et al. (2010) suggest that a gravity wave which is emitted from the parent storm played a part in the development of deep convection in the daughter. In the model simulations two pronounced waves are emitted from the parent storm between 06 and 09Z on the 31st. The first wave is emitted from the parent storm at approximately 06Z, it propagates towards the northwest and reaches the region of shallow convection associated with the daughter storm at 11Z. This wave generates shallow cloud at the initiation location of the daughter storm but does not initiate deep convection. The second wave is emitted from the parent storm at approximately 09Z and reaches the daughter storm at 13Z. Boundary-layer mixing is more intense by this time and the arrival of the wave coincides exactly with the development of deep convection in the daughter storm.

Both these waves appear to be wave-fronts that propagate throughout the depth of the free troposphere, rather than a bore-like wave which Taylor et al. (2010) suggest may have propagated along the stable interface between the convective boundary layer and near-neutral Saharan Air Layer aloft. The model waves cause upward displacement of air in the lower half of the troposphere and downward displacement of air in the upper troposphere. This suggests that the waves are of n=2 mode, with a vertical wavelength equal to the depth of the troposphere. This interpretation is supported by weaker evidence of a deep n=1 mode in the

model, which travels approximately twice as fast as the n=2 waves that trigger the convection.

This study suggests that there are three aspects which need to be accurately represented in a model in order to be able to predict this kind of system. Firstly, the large-scale circulation and thermodynamic profile must be representative, which requires a good quality atmospheric analysis to initialise the forecast. Secondly, if the location of the initiation of the system is to be forecast accurately, the spatial variability of land surface properties (notably soil moisture) must be accurate. Finally, in order to reproduce the timing of secondary initiation correctly the model must be able to capture gravity waves that are emitted by existing systems.

Acknowledgements

The authors would like to thank Caroline Bain, Sean Milton and Bethan White for fruitful discussions and suggestions and two anonymous reviewers for their helpful comments and suggestions. We are grateful to the National Centre for Atmospheric Science (NCAS) Computer Modelling Service for help with model configurations, initialisation data and general enquires. We would like to thank EUMETSAT for the cloud data, Le Laboratorie de Météorologie Dynamique for the EPSAT-SG precipitation data and Thierry Pellarin for the AMSR-E/EPSAT-SG surface soil moisture product. We also acknowledge the TRMM mission scientists and associated NASA personnel for the production of the TRMM data used in this paper and are grateful to the Goddard Earth Sciences Data and Information Services Center (GES DISC) for making the data available. The work has been supported by NERC Grants NE/B505538/1, NE/G018499/1 and NE/E003826/1. Based on a French initiative, AMMA was built by an international scientific group and is currently funded by a large number of agencies, especially from France, UK, US and Africa. It has been the beneficiary of a major financial contribution from the European Community's Sixth Framework

Research Programme. Detailed information on scientific coordination and funding is available on the AMMA International web site http://www.ammainternational.org.

References

Adler B, Kalthoff N, Gantner L. 2011. The impact of soil moisture inhomogeneities on the modification of a mesoscale convective system: An idealised model study. *Atmos. Res.* **101**: 354–372.

Agustí-Panareda A, Balsamo G, Beljaars A. 2010a. Impact of improved soil moisture on the ECMWF precipitation forecast in West Africa. *Geophys. Res. Lett.* **37**: L20808, doi:10.1029/2010GL044748.

Agustí-Panareda A, Beljaars A, Ahlgrimm M, Balsamo G, O B, Forbes R, Ghelli A, Guichard F, K¨ohler Meynadier R, Morcrette JJ. 2010b. The ECMWF re-analysis for the AMMA observational campaign. *Q. J. R. Meteorol. Soc.* **136**: 1457–1472.

Agustí-Panareda A, Beljaars A, Cardinali C, Genkova I. 2010c. Impacts of assimilating AMMA soundings on ECMWF analyses and forecasts. *Wea. Forecasting* **25**: 1142–1160.

Anabor V, Stensrud DJ, de Moraes OLL. 2009. Simulation of a serial upstream-propagating mesoscale convective system event over southeastern South America using composite initial conditions. *Mon. Weat. Rev.* **137**: 2144–2163.

Bergés JC, Jobard L, Chopin F, Roca R. 2010. EPSAT-SG: a satellite method for precipitation estimation; its concepts and implementation for the AMMA experiment. *Ann. Geophys.* **28**: 289–308.

Beres JH, Alexander MJ, Holton JR. 2002. Effects of tropospheric wind shear on the spectrum of convectively generated gravity waves. *J. Atmos. Sci.* **59**: 1805–1824.

Best MJ, coauthors. 2011. The Joint UK Land Environment Simulator (JULES), model description - Part 1: Energy and water fluxes. *Geosci. model Dev.* **4**: 677–699.

Boone A, de Rosnay P, Balsamo G, Beljaars A, Chopin F, Decharme B, Delire C, Ducharne A, Gascoin S, Grippa M, Guichard F, Gusev Y, Harris P, Jarlan L, Kergoat L, Mougin E, Nasonova O, Norgaard A, Orgeval T, Ottlé C, Poccard-Leclercq Polcher J, Sandholt I, Saux-Picart S, Taylor C, Xue Y. 2009. The AMMA land surface model intercomparison project (ALMIP). *Bull. Am.Meteor. Soc.* **90**: 1865–1880.

Bretherton CS, Smolarkiewicz PK. 1989. Gravity waves, compensating subsidence and detrainment around cumulus clouds. *J. Atmos. Sci.* **46**: 740–759.

Carleton AM, Adegoke J, Allard J, Arnold DL, Travis DJ. 2001. Summer season land cover - Convective cloud associations for the Midwest US 'Corn Belt'. *Geophys. Res. Lett.* **28**: 1679–1682.

Charba J. 1974. Application of gravity current model analysis of squall-line gust front. *Mon. Weat. Rev.* **102**: 140–156.

Crook NA, Miller MJ. 1985. A numerical and analytical study of atmospheric undular bores. *Q. J. R. Meteorol. Soc.* **111**: 225–242.

Davies T, Cullen MJP, Malcolm AJ, Mawson MH, Staniforth A, White AA, Wood S. 2005. A new dynamical core for the Met Office's global and regional modelling of the atmosphere. *Quart. J. Roy. Meteor. Soc.* **131**: 1759–1782.

Droegemeier KK, Wilhelmson RB. 1985a. Three-dimensional numerical modeling of convection produced by interacting thunderstorm outflows. Part I: Control simulation an d low-level moisture variations. *J. Atmos. Sci.* **42**: 2381–2403.

Droegemeier KK, Wilhelmson RB. 1985b. Three-dimensional numerical modeling of convection produced by interacting thunderstorm outflows. Part II: Variations in vertical winds shear. *J. Atmos. Sci.* **42**: 2404–2414.

Emanuel KA. 1994. *Atmospheric Convection*. Oxford University Press.

Emori S. 1998. The interaction of cumulus convection with soil moisture distribution: An idealized simulation. *J. Geophys. Res.* **103**: 8873–8884.

Essery RLH, Best MJ, Cox PM. 2001.MOSES 2.2 technical documentation. Technical report, Met Office. 14 August 2001.

Gaertner MA, Domíguez M, Garvert M. 2010. A modelling case-study of soil moisture-atmosphere coupling. *Q. J. R. Meteorol. Soc.* **136**: 483–495.

Gantner L, Kalthoff N. 2010. Sensitivity of a modelled life cycle of a mesoscale convective system to soil conditions over West Africa. *Q. J. R. Meteorol. Soc.* **136**: 471–482.

Garcia-Carreras L, Parker DJ, Marsham JH. 2011. What is the mechanism for the modification of convective cloud distributions by land surface-induced flows? *J. Atmos. Sci.* **68**: 619–634.

Goff RC. 1976. Vertical structure of thunderstorm outflows. *Mon. Weat. Rev.* **104**: 1429–1440.

Goler RA, ReederMJ. 2004. The generation of the Morning Glory. *J. Atmos. Sci.* **61**: 1360–1376.

Gregory D, Rowntree PR. 1990. A mass flux convection scheme with representation of cloud ensemble characteristics and stability-dependent closure. *Mon. Wea. Rev.* **118**: 1483–1506.

Guichard F, coauthors. 2010. An intercomparison of simulated rainfall and evapotranspiration associated with a mesoscale convective system over West Africa. *Journal of Hydrometeorology* **25**: 37–60.

Janicot S, Thorncroft CD, Ali A, Asencio N, Berry G, Bock O, Bourles B, Caniaux G, Chauvin F, Deme A, Kergoat L, Lafore JP, Lavaysse C, Lebel T, Marticorena B, Mounier F, Nedelec P, Redelsperger JL, Ravegnani F, Reeves CE, Roca R, de Rosnay P, Schlager H, Sultan B, Tomasini M, Ulanovsky A, forecasters team A. 2008. Large-scale overview of the summer monsoon over West Africa during the AMMA field experiment in 2006. *Ann. Geophys.* **26**: 2569–2595.

Hourdin F, coauthors. 2010. AMMA-Model intercomparison project. *Bull. Am. Meteorol. Soc.* **91**: 95–104.

Huffman G.J, Adler RF, Bolvin DT, Gu G. Nelkin EJ, Bowman KP, Hong Y, Stocker EF, Wolff DB. 2007. The TRMM Multi-satellite Precipitation Analysis: Quasi-Global, Multi-Year, Combined-Sensor Precipitation Estimates at Fine Scale. *J. Hydrometeor.* **8**: 38-55.

Klüpfel V, Kalthoff N, Gantner L, Kottmeier C. 2011a. Evaluation of soil moisture ensemble runs to estimate precipitation variability in convection permitting model simulations for West Africa. *Atmos. Res.* **101**: 178-193.

Klüpfel V, Kalthoff N, Gantner L, Taylor C. 2011b. Convergence zones and their impact on the initiation of a mesoscale convective system in West Africa. *Q. J. R. Meteorol. Soc.* **138**: 950-963.

Knupp KR. 2006. Observational analysis of a gust front to bore to solitary wave transition within an evolving nocturnal boundary layer. *J. Atmos. Sci.* **63**: 2016–2035.

Koch SE, Feltz W, Fabry F, Pagowski M, Geerts B, Bedka KM, Miller DO, Wilson JW. 2008. Turbulent mixing processes in atmospheric bores and solitary waves deduced from profiling systems and numerical simulation. *Mon. Weat. Rev.* **136**: 1373–1400.

Kohler M, Kalthoff N, Kottmeier C. 2010. The impact of soil moisture modifications on CBL characteristics in West Africa: A case-study from the AMMA campaign *Q. J. R. Meteorol. Soc.* **136**: 442–455.

Koster RD, Dirmeter PA, Guo Z, Bonan G, Chan E, Cox P, Gordon CT, Kanae S, Kowalczyk E, Lawrence D, Liu P, Lu CH, Malyshev S, McAvaney B, Mitchell K, Mocko D, Oki T, Oleson K, Pitman A, Sud YC, Taylor CM, Verseghy D, Vasic R, Xue Y, Yamada T. 2004. Regions of strong coupling between soil moisture and precipitation. *Science* **305**: 1138–1140.

Lac C, Lafore JP, Redelsperger JL. 2002. Role of gravity waves in triggering deep convection during TOGA COARE. *J. Atmos. Sci.* **59**: 1293–1316.

Lane TP, Reeder MJ. 2001. Convectively generated gravity waves and their effect on the cloud environment. *J. Atmos. Sci.* **58**: 2427–2440.

Lane TP, Zhang F. 2011. Coupling between gravity waves and tropical convection at mesoscale. *J. Atmos. Sci.* **68**: 2582-2598.

Laurent H, D'Amato N, Lebel T. 1998. How important is the contribution of the mesoscale convective complexes to the Sahelian rainfall? *Phys. Chem. Earth* **23**: 629–633.

Lin YL, Deal RL, Kulie MS. 1998. Mechanisms of cell regeneration, development, and propagation within a two-dimensional multicell storm. *J. Atmos. Sci.* **55**: 1867–1886.

Liu C, Moncrieff MW. 2004. Effects of convectively generated gravity waves and rotation on the organization of convection. *J. Atmos. Sci.* **61**: 2218–2227.

Lock AP, Brown AR, Bush MR, Martin GM, Smith RNB. 2000. A new boundary layer mixing scheme. Part I: Scheme description and single-column model tests. *Mon. Wea. Rev.* **128**: 3187–3199.

Lothon M, Campistron B, Chong M, Couvreux F, Guichard F, Rio C, Williams E. 2011. Life cycle of a mesoscale circular gust front observed by a C-Band dopplar radar in West Africa. *Mon. Weat. Rev.* **139**: 1370–1388.

Mapes BE. 1993. Gregarious tropical convection. *J. Atmos. Sci.* **50**: 2026–2037.

Marsham JH, Parker DJ. 2006. Secondary initiation of multiple bands of cumulonimbus over southern Britain. II: Dynamics of secondary initiation. *Q. J. R. Meteorol Soc.* **132**: 1053–1072.

Mathon V, Laurent H, Lebel T. 2002. Mesoscale convective system rainfall in the Sahel. *J. Appl. Meteor.* **41**: 1081–1092.

Meynadier R, Bock O, Gervois S, Guichard F, Redelsperger JL, Agustí-Panareda A, Beljaars A. 2010. West African Monsoon water cycle: 2. Assessment of numerical weather prediction water budgets. *J. Geophys. Res.* **115**: D19 105, doi:10.1029/2010JD013 919.

Morcrette C, Browning K, Blyth AM, Bozier KE, Clark PA, Ladd D, Norton EG, Pavelin E. 2006. Secondary initiation of multiple bands of cumulonimbus over southern Britain. I: An observational case-study. *Q. J. R. Meteorol. Soc.* **132**: 1021–1051.

Mueller CK, Carbone RE. 1987. Dynamics of a thunderstorm outflow. *J. Atmos. Sci.* **44**: 1879–1898.

Negri AJ, Adler RF, Xu L, Surratt J. 2004. The impact of Amazonian deforestation on dry season rainfall. *J. Climate* **17**: 1306–1319.

Pellarin T, Tran T, Cohard JM, Galle S, Laurent JP, de Rosnay P, Vischel T. 2009. Soil moisture mapping over West Africa with a 30-min temporal resolution using AMSR-E observations and a satellite-based rainfall product. *Hydrol. Earth Syst. Sci.* **12**: 1887–1896.

Pfister L, Chan KR, Bui TP, Bowen S, Legg M, Gary B, Kelly K, Proffitt M, Starr W. 1993. Gravity waves generated by a tropical cyclone during the STEP tropical field program: A case study. *J. Geophys. Res.* **98**: 8611– 8638.

Piani C, Durran D, Alexander MJ, Holton JR. 2000. A numerical study of three-dimensional gravity waves triggered by deep tropical convection and their role in the dynamics of the QBO. *J. Atmos. Sci.* **57**: 3689–3702.

Raymond DJ. 1983. A forced gravity wave model of self-organizing convection. *J. Atmos. Sci.* **44**: 3528–3543.

Redelsperger JL, Thorncroft CD, Diedhiou A, Lebel T, Parker DJ, Polcher J. 2006. African Monsoon Multidisciplinary Analysis. An international research project and field campaign. *Bull. Amer. Met. Soc.* **87**: 1739–1746.

Ross AN, Tompkins AM, Parker DJ. 2004. Simple models of the role of surface fluxes on convective cold pool evolution. *J. Atmos. Sci.* **61**: 1582– 1595.

Rottman JW, Simpson JE. 1989. The formation of internal bores in the atmosphere: A laboratory model. *Q. J. R. Meteorol. Soc.* **115**: 941–963.

Segal M, Arritt RW. 1992. Nonclassical mesoscale circulations caused by surface sensible heat-flux

gradients. *B. Am. Meteorol. Soc.* **73**(10): 1593–1604.

Smith RK. 1988. Travelling waves and bores in the lower atmopshere: The ”morning glory” and related phenomena. *Earth-Sci. Rev.* **25**: 267–290.

Song IS, Chun HY, Lane TP. 2003. Generation mechanisms of convectively forced internal gravity waves and their propagation to the stratosphere. *J. Atmos. Sci.* **60**: 1960– 1980.

Stensrud DJ, Fritsch JM. 1993. Mesoscale convective systems in weakly forced large-scale environments. Part I: Observations. *Mon. Weat. Rev.* **121**: 3326–3344.

Stensrud DJ, Fritsch JM. 1994. Mesoscale convective systems in weakly forced large-scale environments. Part III: Numerical simulations and implications for operational forecasting. *Mon. Weat. Rev.* **122**: 2084–2104.

Stephens GL, L'Ecuyer T, Forbes R, Gettlemen A, Golaz JC, Bodas-Salcedo A, Suzuki K, Gabriel P, Haynes J. 2010. Dreary state of precipitation in global models. *J. Geophys. Sci.* **115**: D24 211, doi:10.1029/2010JD014532.

Stobie JG, Einaudi F, Uccellini LW. 1983. A case study of gravity wave-convective storms interaction: 9 May 1979. *J. Atmos. Sci.* **40**: 2804–2830.

Taylor CM, Clark DB. 2001. The diurnal cycle and African easterly waves: A land surface perspective. *Q. J. R. Meteorol. Soc.* **127**: 845–867.

Taylor CM, Ellis RJ. 2006. Satellite detection of soil moisture impacts on convection at the mesoscale. *Geophys. Res. Let.* **33**: L03404, doi:10.1029/2005GL025252.

Taylor CM, Gounou A, Guichard F, Harris PP, Ellis RJ, Coureux F, De Kauwe M. 2011. Frequency of Sahelian storm initiation enhanced over mesoscale soil-moisture patterns. *Nature Geoscience* **4**: 430–433.

Taylor CM, Harris PP, Parker DJ. 2010. Impact of soil moisture on the development of the Sahelian mesoscale convective system: A case-study from the AMMA Special Observing Period. *Q. J. R. Meteorol. Soc.* **136**: 456–470.

Taylor CM, Lebel T. 1998. Observational evidence of persistent convective-scale rainfall patterns. *Mon. Weat. Rev.* **126**: 1597–1607.

Taylor CM, Saïd F, Lebel T. 1997. Interactions between the land surface and mesoscale rainfall variability during HAPEX-Sahel. *Mon. Weat. Rev.* **125**: 2211–2227.

Taylor CM, Parker DJ, Harris PP. 2007. An observational case study of mesoscale atmospheric circulations induced by soil moisture. *Geophys. Res. Lett.* **34**: L15801, doi:10.1029/2007GL030572.

Timouk F, coauthors. 2009. Response of sensible heat flux to water regime and vegetation development in a central Sahelian landscape. *J. Hydrology* **375**: 178–189.

Tompkins AM. 2001. Organisation of tropical convection in low wind shears: The role of cold pools. *J. Atmos. Sci.* **58**: 1650-1672.

Trigo IF, Monteiro IT, Olesen F, Kabcsh E. 2008. An assessment of remotely sensed land surface temperature. *J. Geophys. Res.* **113**: D17 108, doi:10.1029/2008JD010035.

Uccellini LW, Koch SE. 1987. The synoptic setting and possible energy sources for mesoscale wave disturbances. *Mon. Weat. Rev.* **115**: 721–729.

Wang J, Chagnon FJF, Williams ER, Betts AK, Renno NO, Machado LAT, Bisht G, Knox R, Brase RL. 2009. Impact of deforestation in the Amazon basin on cloud climatology. *Proc. Natl. Acad. Sci.* **106**: 3670–3674.

Wilson DR, Ballard SP. 1999. A microphysically based precipitation scheme for the U.K. Meteorological Office Unified Model. *Quart. J. Roy. Meteor. Soc.* **125**: 1607–1636.

Wolters D, van Heerwaarden CC, Vil´a-Guerau de Arellano J Cappelaere B, Ramier D. 2010. Effects of soil moisture gradients on the path and the intensity of a West African squall line. *Q. J. R. Meteorol. Soc.* **136**: 2162–2175.

Xue M, Xu Q, Droegemeier KK. 1997. A theoretical and numerical study of density currents in non-constant shear flows. *J. Atmos. Sci.* **54**: 1998–2019.

Yang GY, Slingo J. 2001. The diurnal cycle in the tropics. *Mon. Weat. Rev.* **129**: 784–801.

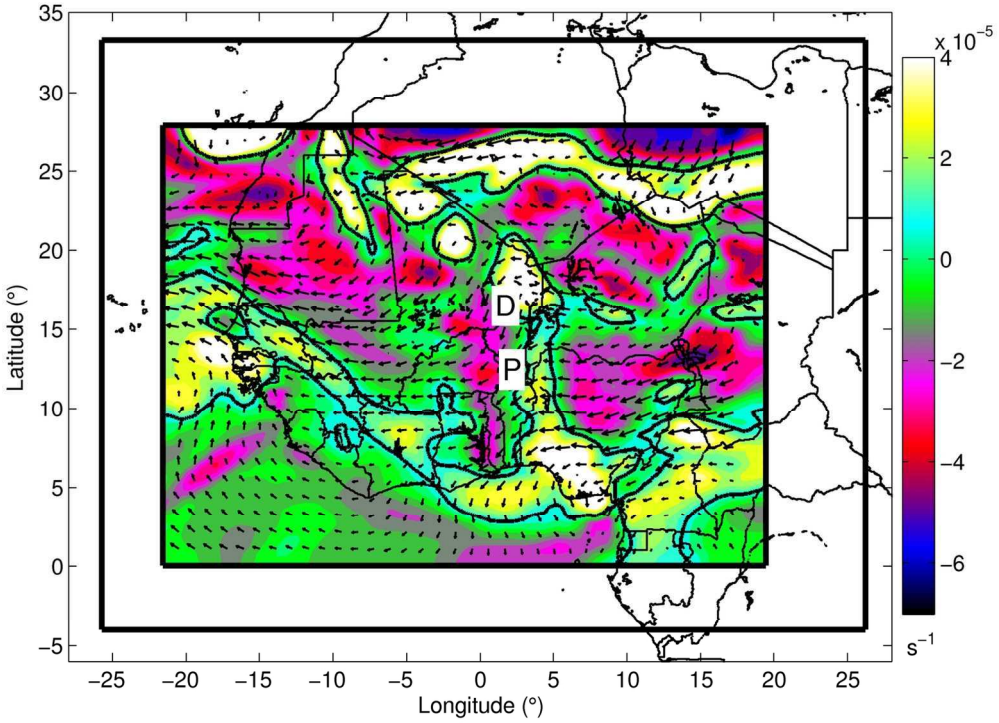

Figure 1 Relative vorticity (shading) and wind vectors at 700 hPa at 12Z, 31st July 2006 from the control run 4 km nest. The thick black line marks the 10-5 s-1 relative vorticity contour. The domain sizes of the 4 and 12 km nests are illustrated by the two black boxes. The locations of the daughter and parent storms at 12Z, 31st July 2006 are marked by the 'D' and 'P'.
140x102mm (300 x 300 DPI)

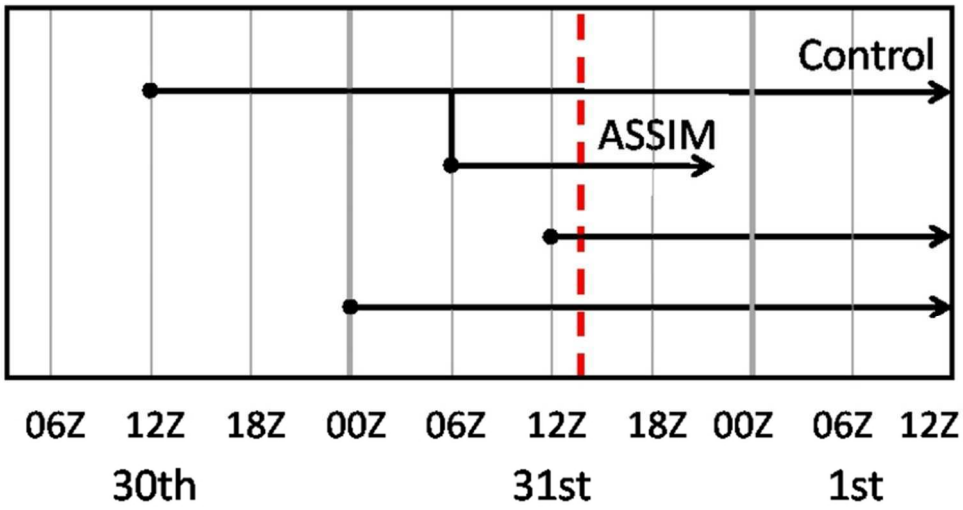

Figure 2 Diagram illustrating the model simulations performed at 4 km horizontal resolution. The red dashed line marks the initiation time of the daughter storm.
72x37mm (300 x 300 DPI)

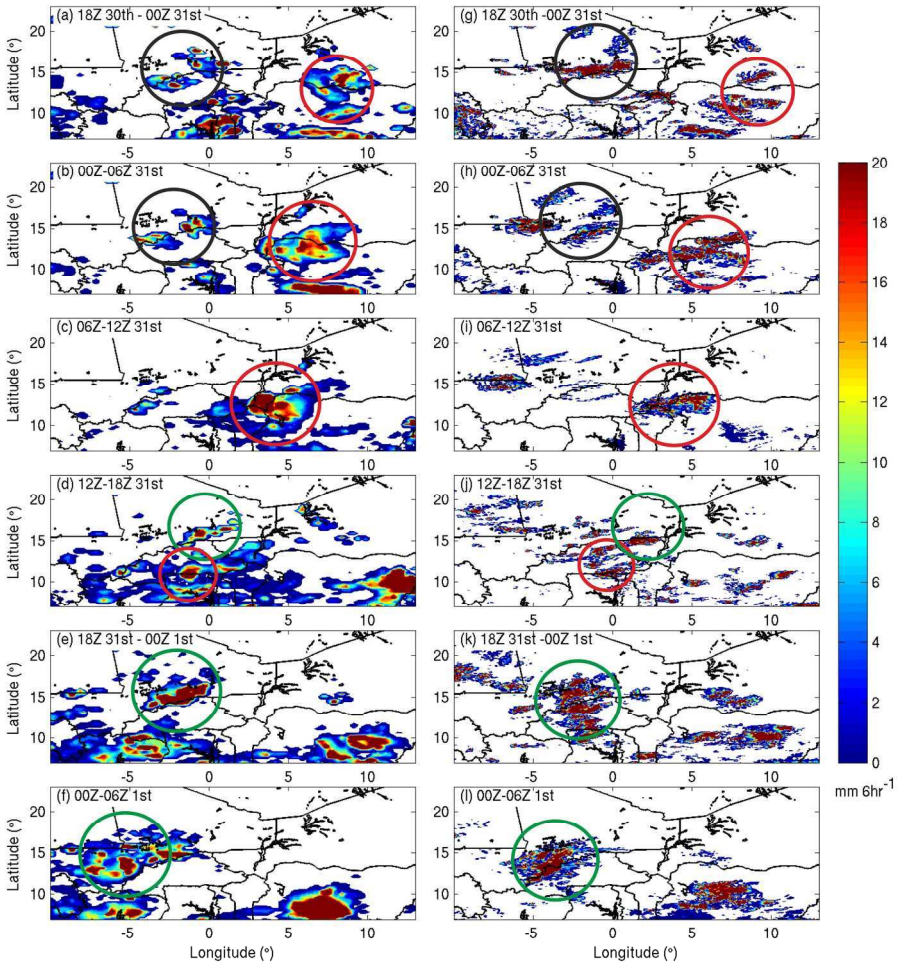

Figure 3 6-hourly accumulated precipitation (mm 6hr^{-1}) from TRMM3B42 (a-f) and the model control run (g-l) from 18Z 30th July 2006 to 06Z 1st August 2006. The black circles mark the MCS on the 30th that produced the wet soil patches, the red circles mark the parent storm and the green circles mark the daughter storm.
259x324mm (300 x 300 DPI)

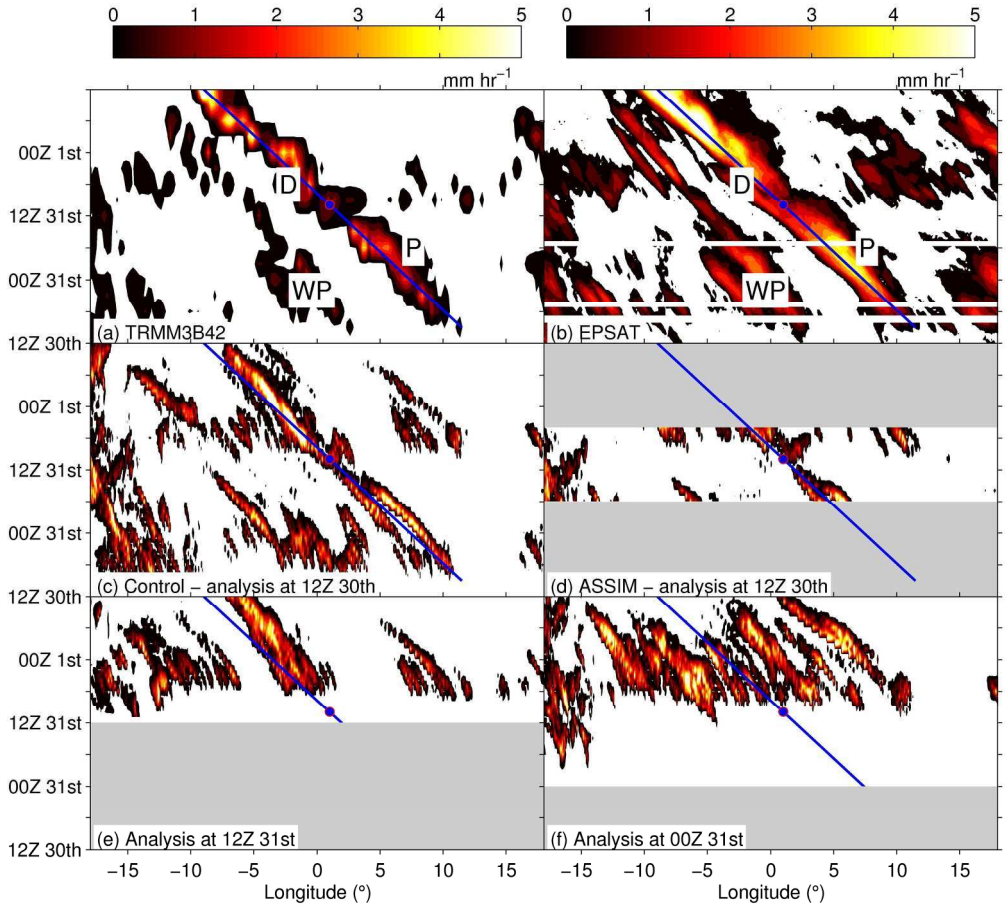

Figure 4 Hovmöller plots of precipitation rate (averaged between 11 and 18°N) for (a) TRMM3B42, (b) EPSAT observations, (c) - (f) various MetUM runs. The blue lines mark the track of the parent (P) and daughter (D) storms in the observations, the storm that produced the wet patches on the 30th is marked by 'WP' in the observations and the blue dots mark the commencement of deep convection in the observations.
203x185mm (300 x 300 DPI)

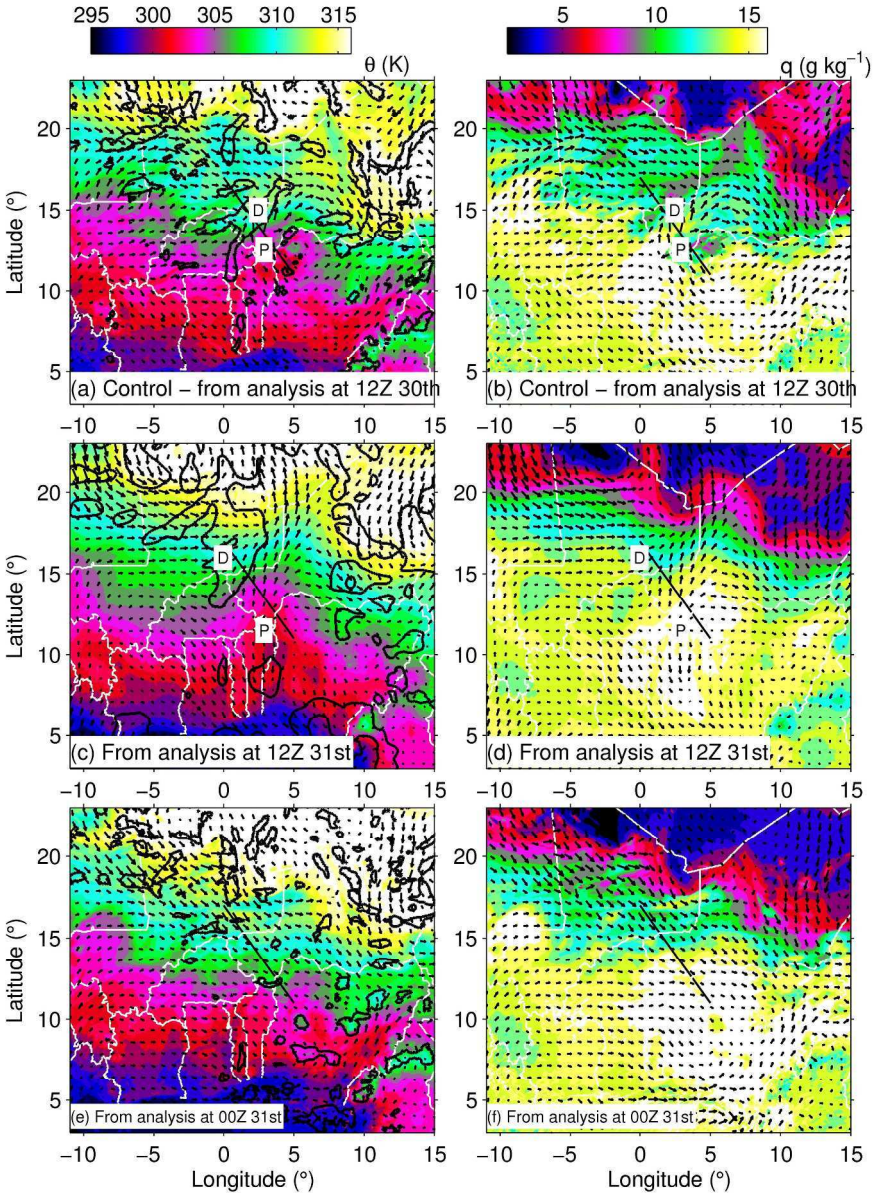

Figure 5 (a), (c) and (e): 925 hPa m potential temperature (shading), a contour of 925 hPa convergence (black lines) and 925 hPa wind vectors for the model simulations initialised at 12Z 30th (control), 12Z 31st and 00Z 31st respectively. The contour of convergence in (a) and (e) is at 3x10-5 s^{-1} and in (c) is at 1x10-5 s^{-1}. (b), (d) and (f): 925 hPa specific humidity (shading) and 925 hPa wind vectors. All model diagnostics are at 12Z, 31st July 2006. The black diagonal line shows the transect used in other plots.
234x318mm (300 x 300 DPI)

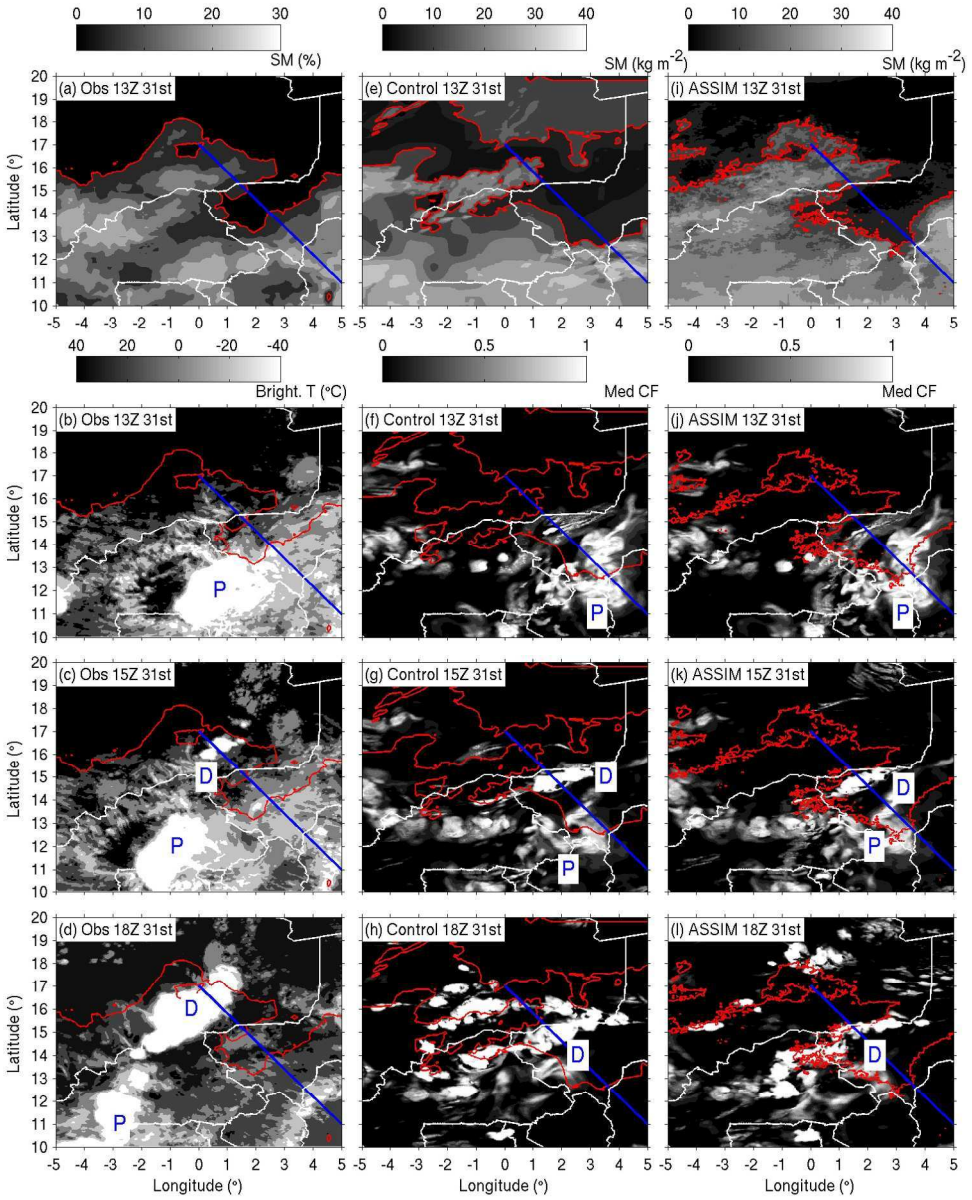

Figure 6 The top panels show soil moisture in the upper-most layer at 13Z, 31st July for (a) the satellite observations, (e) the control simulation and (i) the ASSIM simulation. Note the difference in units between the observed and simulated soil moisture. Panels (b)-(d) show observed soil moisture (red contour at 5 %) and MSG brightness temperatures. Panels (f)-(h) and (j)-(l) show model soil moisture (red contour at 10 kg m^{-2}) and medium cloud fraction (shading). The blue line shows the transect used in the other plots. The blue 'P' and 'D' labels mark the locations of the parent and daughter storms respectively.
239x293mm (300 x 300 DPI)

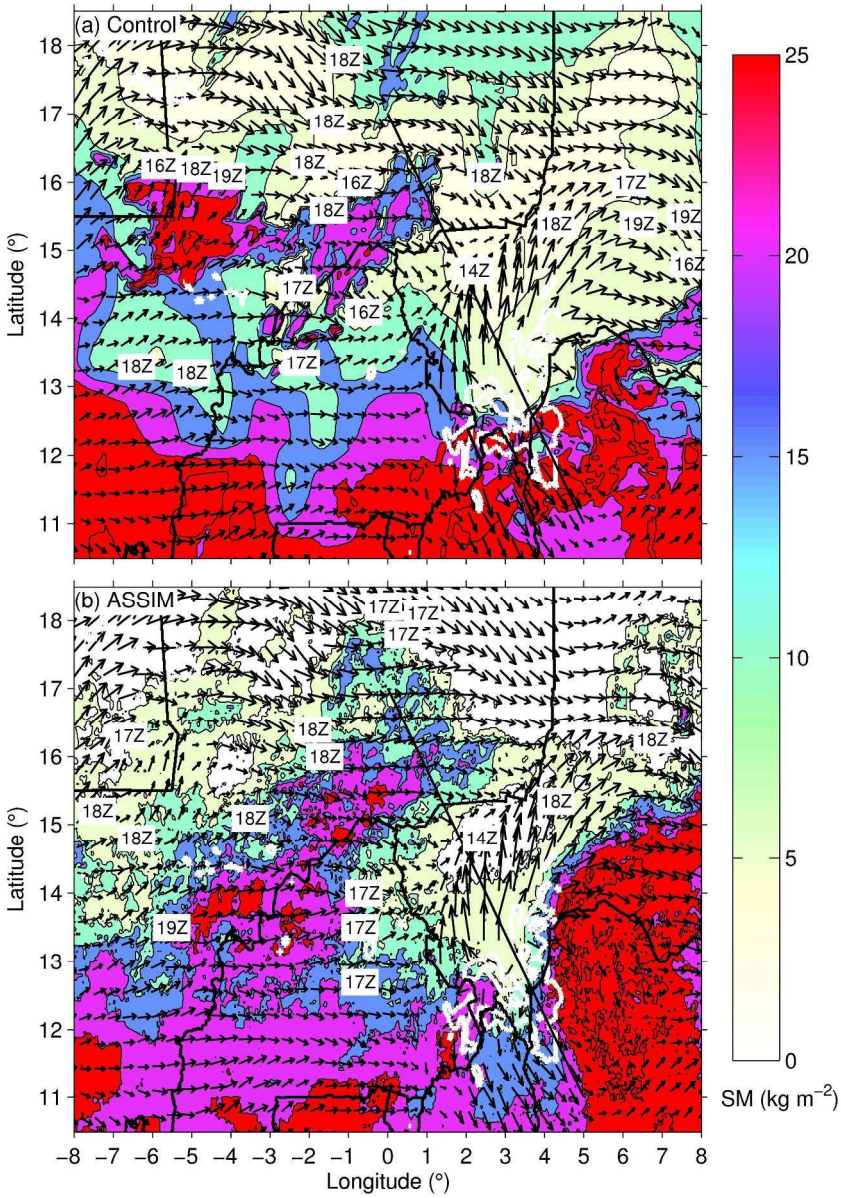

Figure 7 Soil moisture and 925 hPa wind vectors at 12Z, 31st July 2006 from (a) the control run and (b) the ASSIM run at 06Z 31st July 2006. The thick white contour indicates the position of the parent storm at 12Z. The white boxes indicate the locations of the first initiations and contain the times of the first significant rainfall at each location. The black line shows the diagonal transect.
233x330mm (300 x 300 DPI)

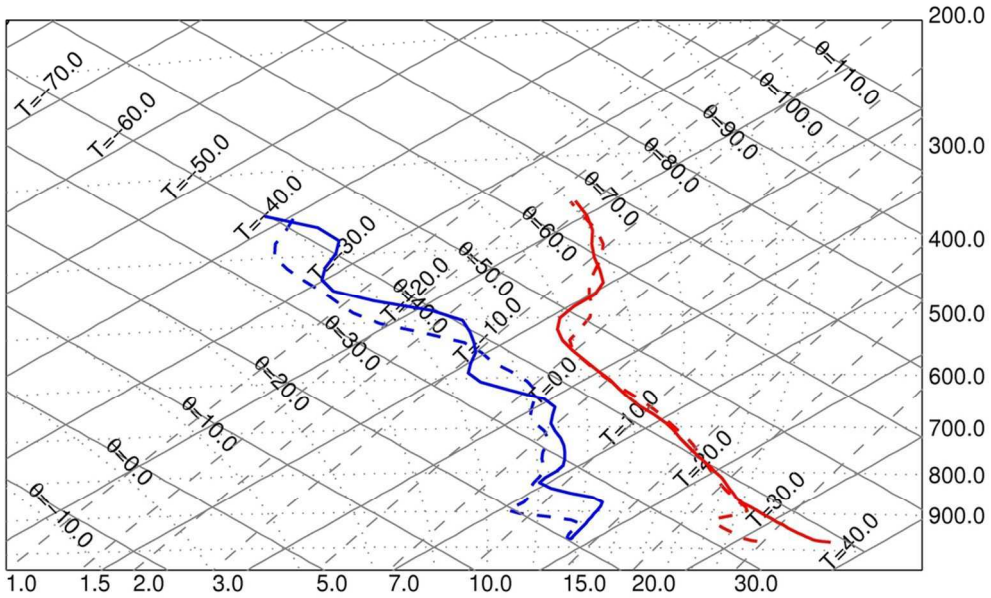

Figure 8 Tephigram of model diagnostics from the control simulation at 11Z, 31st July 2006 over dry soil 15.0°N, 1.7°E, (solid lines) and over the adjacent wet soil at 16.0°N, 1°E for the control run. CAPE values are 1074 J kg^{-1} over the dry soil and 529 J kg^{-1} over the wet soil. CIN values are 16 J kg^{-1} over the dry soil and 163 J kg^{-1} over the wet soil.
94x57mm (300 x 300 DPI)

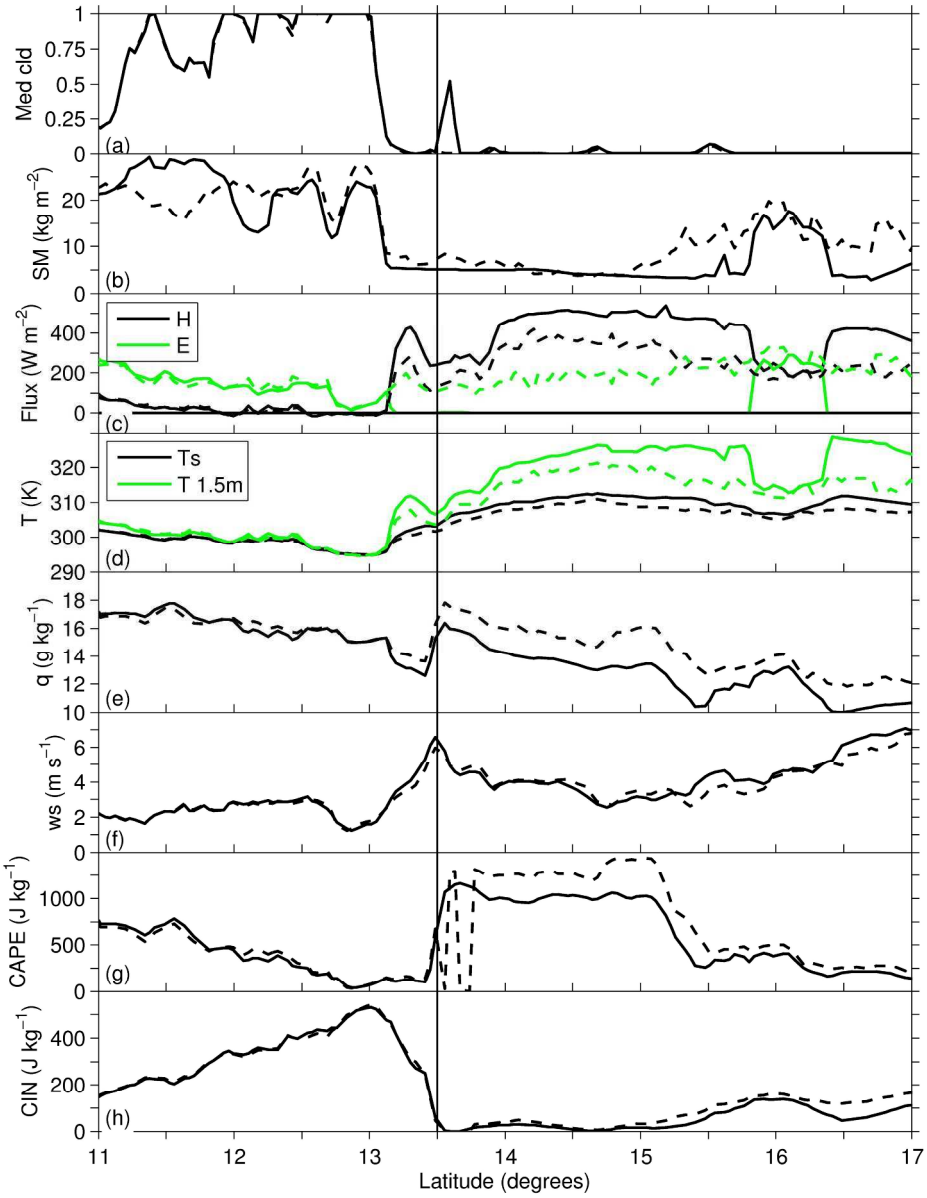

Figure 9 Variables at 11Z, 31st July 2006 along the diagonal: (a) medium cloud fraction, (b) soil moisture in the upper-most layer, (c) surface sensible (H) and latent (E) heat fluxes, (d) surface (Ts) and near-surface (T1.5m) temperatures, (e) near-surface specific humidity, (f) 10 m wind speed, (g) convective available potential energy (CAPE), (h) convective inhibition (CIN). Solid lines represent diagnostics from the control and the dashed lines represent diagnostics from the ASSIM simulation. The vertical black line marks the position of the cold pool on the diagonal section.
240x309mm (300 x 300 DPI)

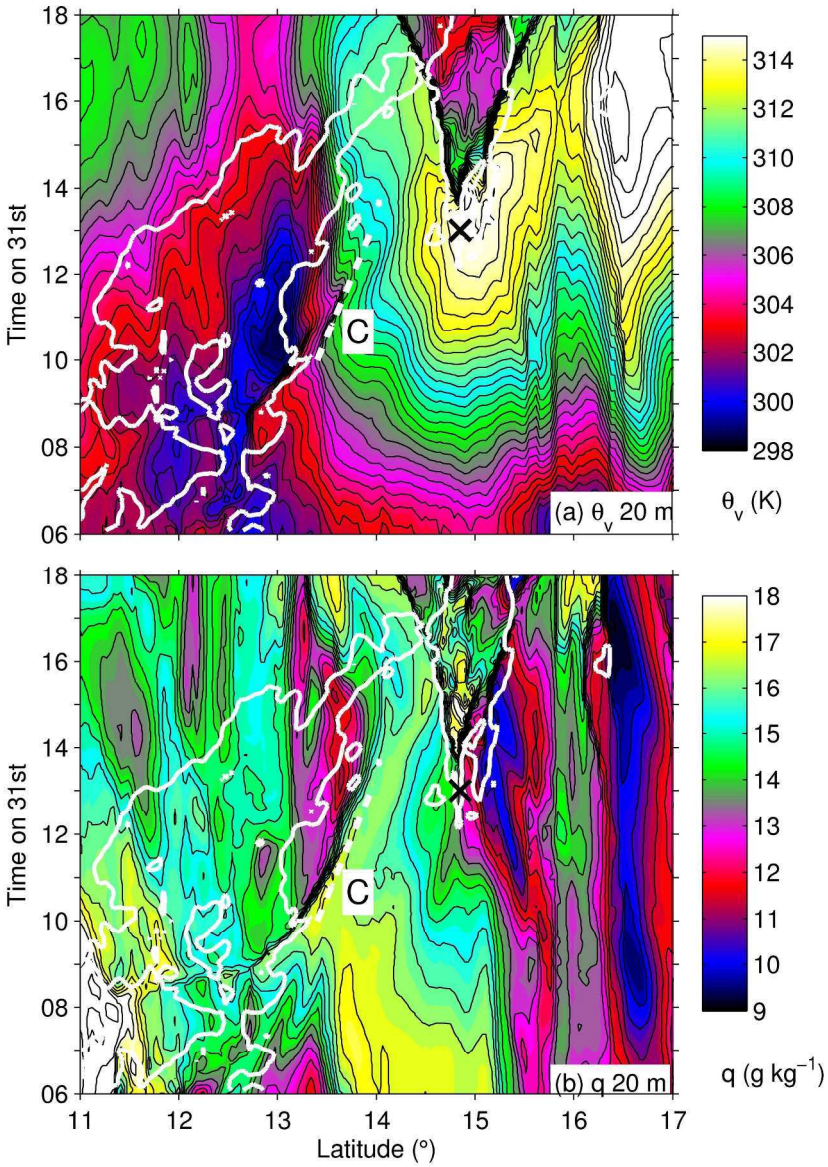

Figure 10 Hovmöller plot of (a) θ_v and (b) specific humidity at 20 m above ground level along the diagonal transect. The thick white contour shows 100 % medium cloud fraction. The dashed white line indicates the propagation of the cold pool (C). The time of the initiation of deep convection in the daughter storm is marked by the black cross.
205x294mm (300 x 300 DPI)

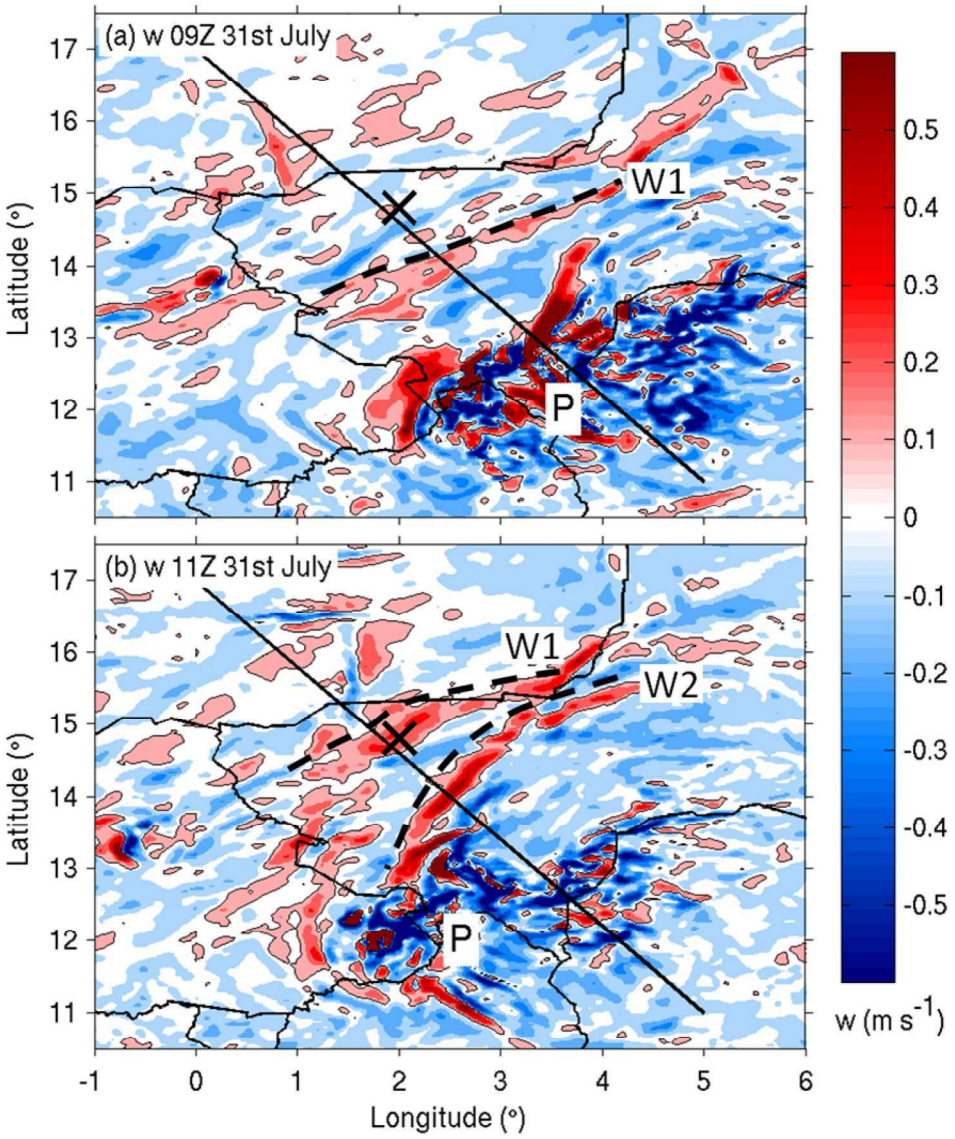

Figure 11 700 hPa vertical velocity at (a) 09Z and (b) 11Z, 31st July 2006. The single black contour is at 0.1 m s^{-1}. The black dashed lines indicate the leading edge of the two waves (W1 and W2). The 'P' indicates the location of the parent storm, the black cross the daughter storm initiation point and the black line the diagonal transect.
185x217mm (300 x 300 DPI)

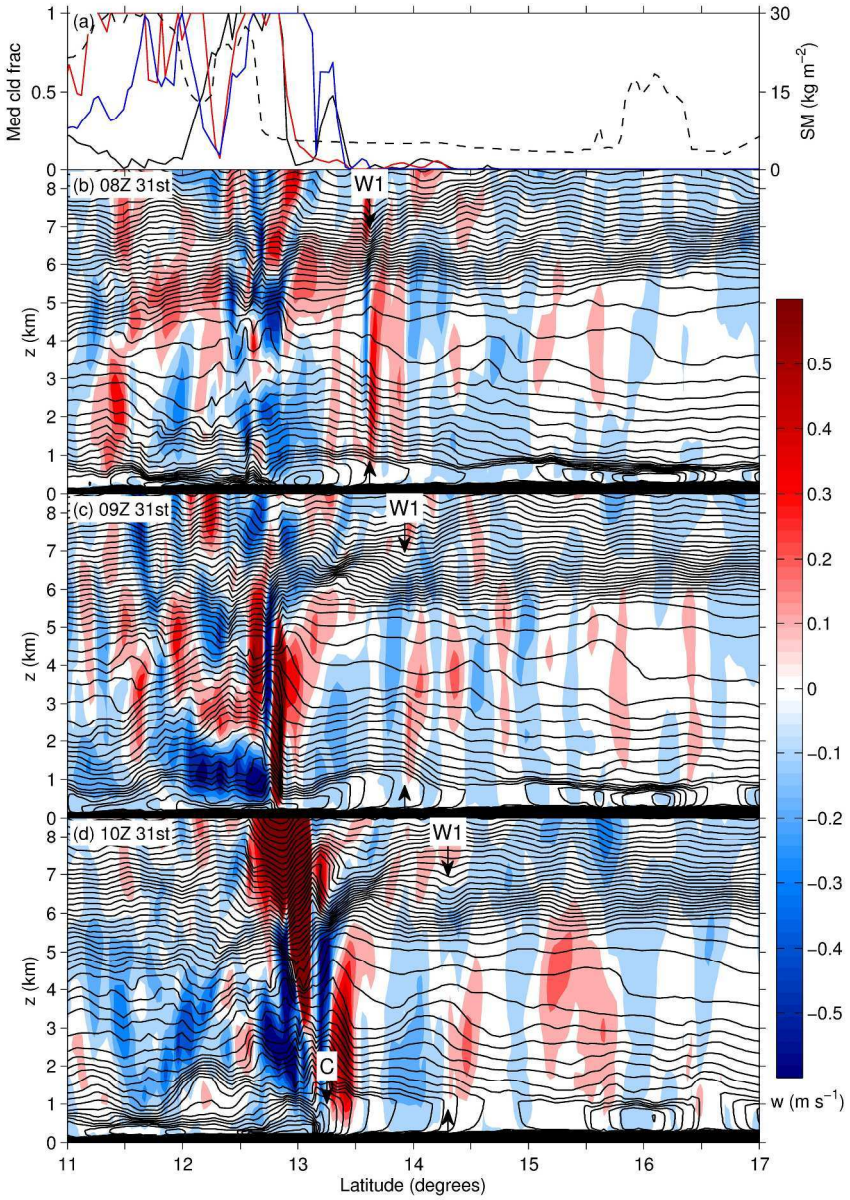

Figure 12 (a) Soil moisture (dashed line) and medium cloud fraction at 08Z (black line), 09Z (red line) and 10Z (blue line) (b)-(d): vertical velocity (shading) and virtual potential temperature (black contours at 0.75 K intervals). All diagnostics are from the control simulations and are along the diagonal transect. The arrows mark the position of the first wave (W1) and the cold pool (C).
281x397mm (300 x 300 DPI)

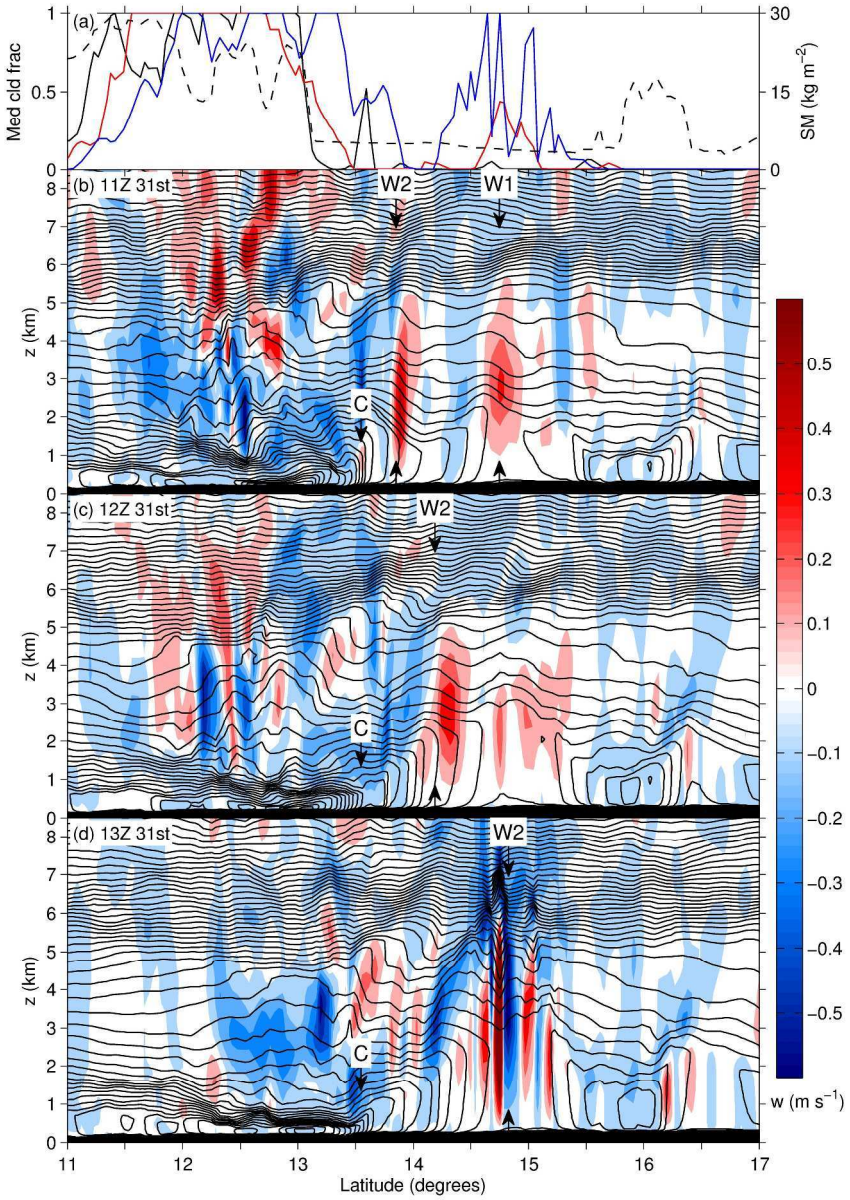

Figure 13 Same as Figure 11 but for 11, 12 and 13Z. The black, red and blue lines in (a) represent the medium cloud fraction at 11, 12 and 13Z respectively.
281x397mm (300 x 300 DPI)

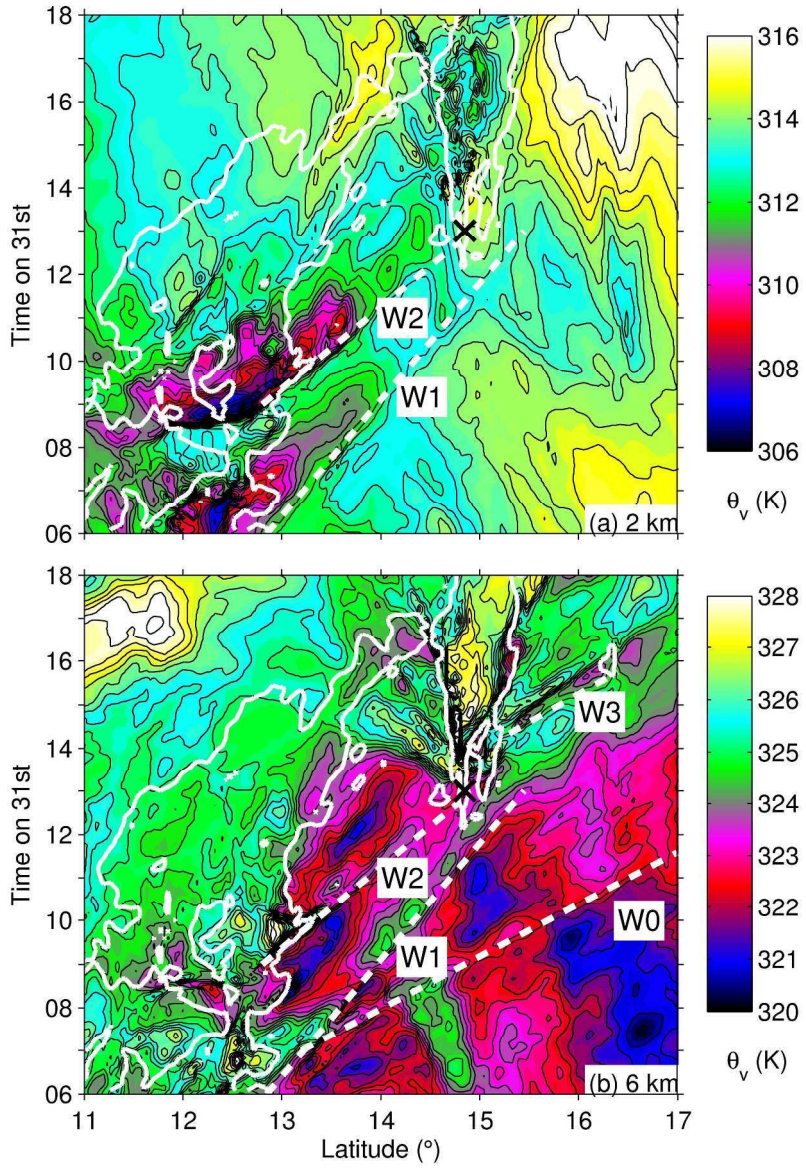

Figure 14 Hovmöller plots of θ_v along the diagonal transect at (a) 2 km and (b) 6 km above mean sea level. The thick white contour shows 100 % medium cloud fraction. The white dashed lines indicate the waves (W0-W4). The time of the initiation of deep convection in the daughter storm is marked by the black cross.
205x306mm (300 x 300 DPI)

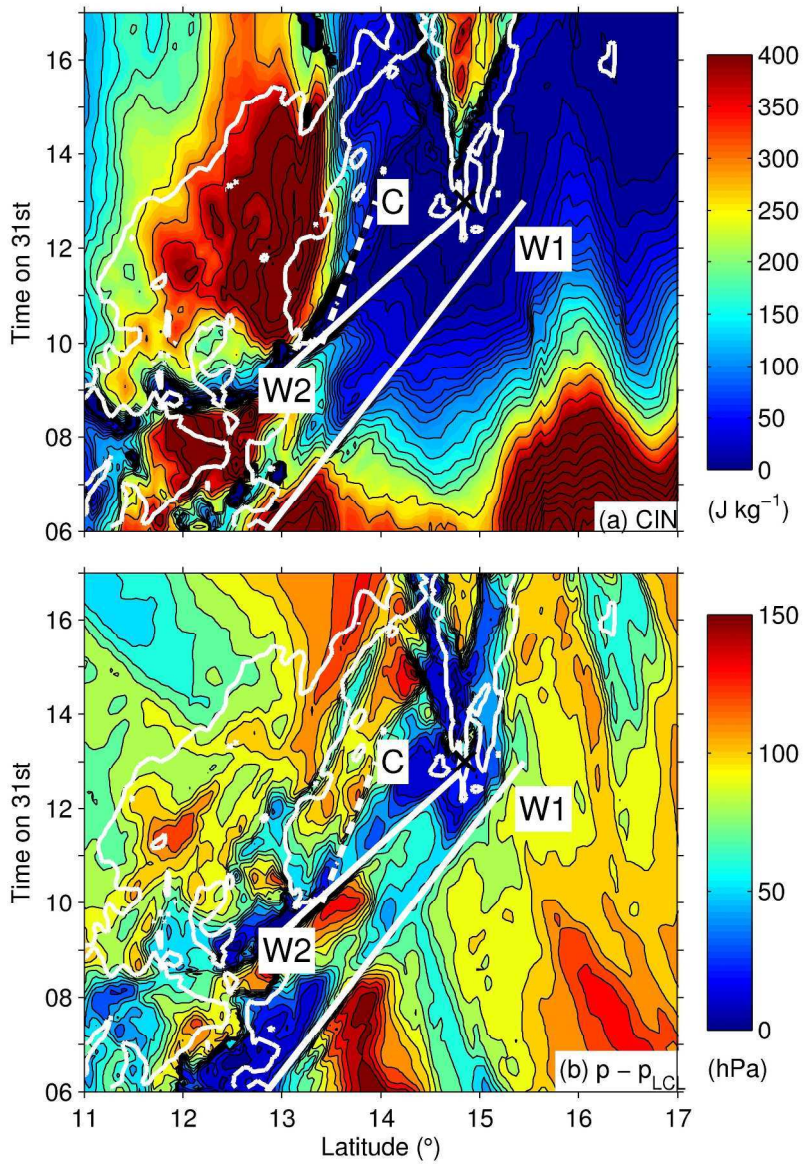

Figure 15 Hovmöller plots along the diagonal transect of (a) CIN, where contours are at 50 J kg^{-1} intervals above 200 J kg^{-1}, at 20 J kg-1 intervals above 100 J kg^{-1} and at 10 J kg^{-1} below 100 J kg^{-1} and (b) the pressure at 3000 m minus the pressure of the lifting condensation level, where contours are at 10 hPa intervals. The thick white contour shows 100 % medium cloud fraction. The dashed white line indicates the propagation of the cold pool (C) and the white lines indicate the two waves (W1 and W2). The time of the initiation of deep convection in the daughter storm is marked by the black cross.
205x306mm (300 x 300 DPI)

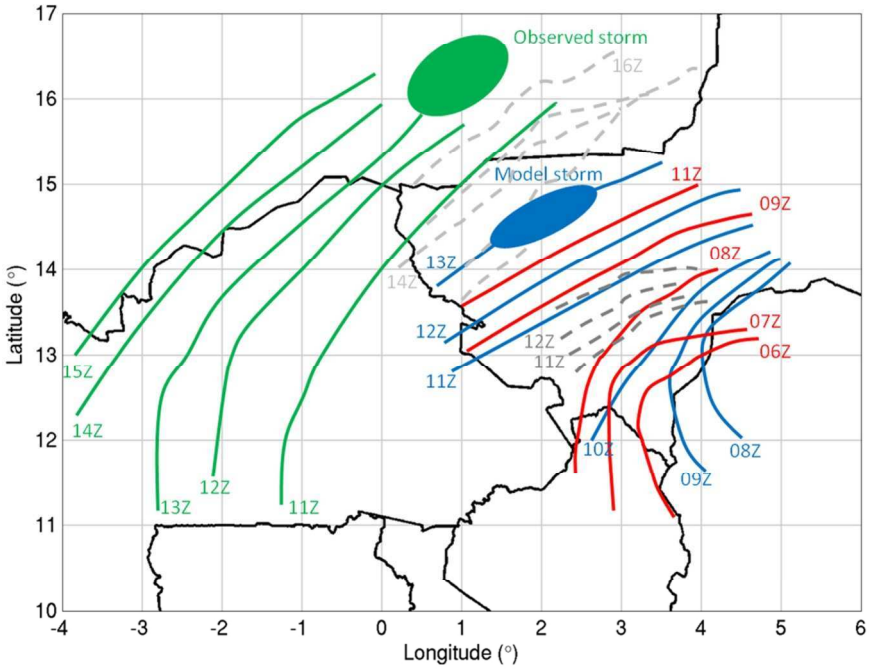

Figure 16 Schematic of the gravity waves and cold pools associated with this case. The observed gravity wave is shown by the solid green lines and the observed cold pool by the light grey dashed lines. The first and second model gravity waves are shown by the solid red and blue lines respectively and the dark grey dashed lines show the model cold pool.
153x114mm (300 x 300 DPI)

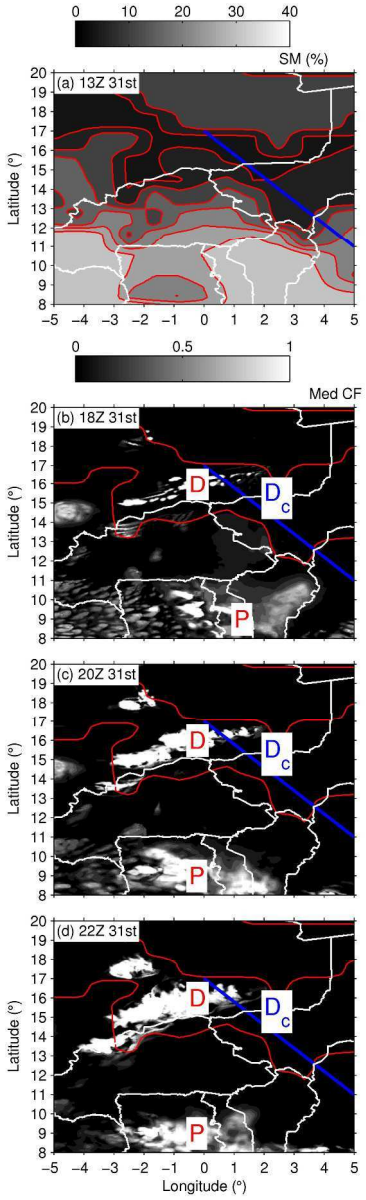

Figure 17 (a) Soil moisture at 13Z, (b)-(d) medium cloud fraction at 18, 20 and 22Z and a contour of soil moisture at 10 kg m^{-2} for the model run initialised at 12Z, 31st July 2006. The blue line marks the diagonal transect used in the analysis of the control. The blue 'D_c' marks the location of the initiation of the daughter storm in the control, the red 'D' and 'P' mark the locations of the daughter and parent storms in this run.
284x926mm (300 x 300 DPI)